

Finite-particle tracking reveals submicroscopic-size changes of mitochondria during transport in mitral cell dendrites

Arne Gennerich^{1,2} and Detlev Schild¹

¹ Department of Neurophysiology and Cellular Biophysics, University of Göttingen, Humboldtallee 23, 37073 Göttingen, Germany

² Department of Cellular and Molecular Pharmacology, University of California San Francisco, San Francisco, CA 94143-2200, USA

E-mail: gennerich@gmail.com and dschild@gwdg.de

Received 12 November 2005


Accepted for publication 23 January 2006

Published 16 February 2006

Online at stacks.iop.org/PhysBio/3/45

Abstract

The mechanisms of molecular motor regulation during bidirectional organelle transport are still uncertain. There is, for instance, the unsettled question of whether opposing motor proteins can be engaged in a tug-of-war. Clearly, any non-synchronous activation of the molecular motors of one cargo can principally lead to changes in the cargo's shape and size; the cargo's size and shape parameters would certainly be observables of such changes. We therefore set out to measure position, shape and size parameters of fluorescent mitochondria (during their transport) in dendrites of cultured neurons using a finite-particle tracking algorithm. Our data clearly show transport-related submicroscopic-size changes of mitochondria. The observed displacements of the mitochondrial front and rear ends are consistent with a model in which microtubule plus- and minus-end-directed motor proteins or motors of the same type but moving along anti-parallel microtubules are often out-of-phase and occasionally engaged in a tug-of-war. Mostly the leading and trailing ends of mitochondria undergo similar characteristic movements but with a substantial time delay between the displacements of both ends, a feature reminiscent of an inchworm-like motility mechanism. More generally, we demonstrate that observing the position, shape and size of actively transported finite objects such as mitochondria can yield information on organelle transport that is generally not accessible by tracking the organelles' centroid alone.

 This article features online supplementary data

Introduction

Most bidirectional long-distance mitochondria transport is thought to be achieved by the microtubule transport system [1, 2]. Transport in the microtubule plus-end direction is driven by motor proteins of the kinesin family, whereas transport in the microtubule minus-end direction is mainly carried out by cytoplasmic dynein [3, 4, 5]. While the properties of single motor proteins have been extensively studied *in vitro* [6], their *in vivo* function and the mechanisms of coordinating

opposite-polarity motors in living cells are as yet poorly understood (reviewed in [7, 8]). Several studies have suggested that opposite-polarity motors can associate with the same cargo simultaneously and that motors with the required directionality become activated while at the same time the activities of motors with opposite directionality are downregulated [9–14]. Such a mechanism must be able to rapidly coordinate the activity of opposing motors to prevent a tug-of-war [10, 15]. Bidirectional organelle transport has been found, indeed, to depend on motor cofactor proteins

such as the protein complex dynactin (e.g. [15–19]) and the regulator proteins Klar [20] and Halo [12]. In addition, phosphorylation/dephosphorylation of motor proteins may play a role in the regulation of bidirectional organelle transport [21–23].

Despite the progress on dissecting the molecular mechanisms underlying bidirectional transport, there is as yet no direct evidence for coordination or tug-of-war between opposing motors [7]. Whereas a mechanism entirely based on competitive activity of opposing motors is unlikely and is not supported by the current state of research [8], a combination of motor coordination and tug-of-war (failed coordination) could potentially explain the oscillatory forward and backward movements of cargos during net unidirectional transport. Direct visualization of the activities of motor proteins while attached to the same cargo is presently not feasible. New biophysical means have to be employed to this end because the commonly observed center-of-mass movement of organelles generally does not allow one to gain direct evidence on the simultaneous activity of opposing motor proteins. Studying positions, shapes and sizes of actively transported finite objects such as mitochondria, on the other hand, could potentially yield direct evidence for movement-related changes in size and shape of transported targets. The simultaneous activity of opposite-polarity motors attached to the front and rear ends of the cargo, respectively, could cause detectable simultaneously opposing motor steps. Such investigations, however, have not been undertaken yet.

Here we made a first step in this direction and examined whether bidirectional transport affects the cargo's shape and size on a submicroscopic-scale level. We applied a recently introduced finite-particle tracking (FPT) algorithm [24] and studied mitochondria transport in dendrites of cultured neurons of *Xenopus laevis* tadpoles. Mitochondria were chosen because these organelles often have ellipsoid- or sausage-like shapes that are easy to analyze with the FPT algorithm. Our investigation reveals, for the first time, transport-induced submicroscopic-size changes of mitochondria. We show that both mitochondrial ends can undergo similar time-delayed characteristic movements. One of the cargo ends seems to dictate the direction and speed of transport while the opposite end is locked-in later and thus lags behind.

In summary, we demonstrate that the FPT analysis of actively transported finite objects such as mitochondria opens a window for studying movement-related size changes and potentially other mechanisms of bidirectional organelle transport in living cells.

Materials and methods

Cell culture and staining of mitochondria

Cultured neurons of the olfactory bulb of *Xenopus laevis* tadpoles were prepared and characterized as previously described [25] (see the supplementary data available from stacks.iop.org/PhysBio/3/45 for details). Living mitochondria were labeled with MitoTracker Orange (Molecular Probes, Leiden, The Netherlands) (see the supplementary data available from stacks.iop.org/PhysBio/3/45 for details).

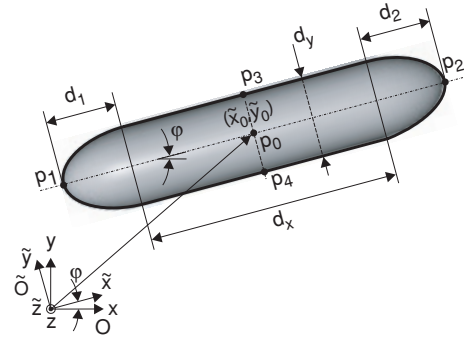


Figure 1. Schematic representation of the three-dimensional ‘sausage-model’. The position of the object within an image is defined by the coordinates $(\tilde{x}_0, \tilde{y}_0)$ given in the rotated coordinate system \tilde{O} , where its orientation is defined by the angle φ with respect to the x -axis of the coordinate system O . Assuming movement in the negative \tilde{x} -direction, the positions of the center, the front end, the rear end, the right border and the left border of the model are given by the points p_0 , p_1 , p_2 , p_3 and p_4 , respectively, with respect to \tilde{O} .

Experimental setup

Measurements were performed using a home-built instrument combining the advantages of fluorescence correlation spectroscopy (FCS) and confocal laser scanning microscopy (CLSM) as previously described [24, 26]. The minimum scanning time per line was set to 1 ms. To allow both fast image acquisition and the observation of long-distance transport processes, the long axis of the dendrite of interest was aligned with the x -axis of the scanning field (corresponds to the scanning direction) by rotating the culture dish around the optical axis.

Finite-particle tracking (FPT) analysis

Position, orientation, shape and size parameters of mitochondria were determined using a recently introduced FPT algorithm [24]. FPT analysis is based on fitting a theoretical intensity distribution $I_{\text{obj}}(x, y, z = 0)$ of a 3D model object to the measured fluorescence image of the organelle. The geometry of the object is modeled by a cylinder with two hemiellipsoidal caps attached to it (figure 1, ‘sausage-model’). Here, we used an approximation of the sausage model by a stack of rectangular slices (see equations (6), (7) and (11) in [24]). The parameters of the algorithm are (figure 1) an amplitude factor p , the length d_1 of the left cap, the length d_2 of the right cap, the length d_x of the cylinder, the cylinder diameter d_y , the angle φ by which the major symmetry axis of the object is rotated around the z -axis (optical axis) with respect to the x -axis of the coordinate system O (coincides with the coordinate system of the CLSM image, see figure 2(a)), the center of the cylinder $p_0 = (\tilde{x}_0, \tilde{y}_0)$ with respect to \tilde{O} and a background constant I_B . The length and width of the object are thus determined by the parameters $d = d_1 + d_x + d_2$ and d_y , respectively. By varying the parameters d_1 , d_2 , d_x and d_y of the underlying model, the object can easily assume the shape of a sausage, ellipsoid or

sphere. However, a precise detection of the object boundaries requires a homogeneous background intensity. Furthermore, caution is necessary when applying the algorithm to images of objects with a component of movement along the optical axis (out-of-focus movement), as a vertically tilted object would appear shorter than it actually is [24]. Hence, we have analyzed experimental examples in which both the average mitochondrial size and the mean mitochondrial intensity were constant over the time course of the measurement. These requirements are typically fulfilled when analyzing transport processes along microtubules oriented parallel and close to the cover slip, as, e.g., in thin axons and dendrites of cultured neurons.

Statistical analysis based on data from two processes

To determine whether the source for detected mitochondrial size fluctuations (quantized by the standard deviation σ_m of the measured mitochondrial length or width, respectively) is the noise inherent in a time-varying fluorescence signal, we performed statistical analysis on the experimental and corresponding simulated data (see the supplementary data available from stacks.iop.org/PhysBio/3/45). In the first step, we simulated a sequence of fluorescence images of a mitochondrion of the same shape and size as the experimental mitochondrion (containing fluorescence-based normal-distributed noise [24]) and being transported with identical mean velocities whereas the shape and size parameters were kept constant. The FPT analysis of the simulated mitochondrion yields the standard deviation σ_s of the noise-induced size fluctuations. Next, we calculated the ratio $\alpha = \sigma_m/\sigma_s$ and estimated the probability P that the ratio σ_m/σ_s can be equal to or larger than α . Here, $P(\sigma_m/\sigma_s) \geq \alpha$ was estimated under the assumption that the underlying numbers of σ_m are independent and identical normal distributed ('null hypothesis'), i.e. that mitochondrial size fluctuations are noise induced only (see the supplementary data available from stacks.iop.org/PhysBio/3/45). We derived an equation based on the null hypothesis to precisely determine the maximum error for a given ratio $\alpha = \sigma_m/\sigma_s$ and the numbers N and M of the data values obtained from both experiment and simulation:

$$P\left(\frac{\sigma_m}{\sigma_s} \geq \alpha\right) < 1 - \frac{2^{1-N/2}}{\Gamma(N/2)} \int_0^{\sqrt{N-1}\alpha R} t^{N-1} e^{-t^2/2} dt + \frac{2^{1-M/2}}{\Gamma(M/2)} \int_0^{\sqrt{M-1}R} t^{M-1} e^{-t^2/2} dt, \quad (1)$$

with Γ being the gamma function. $P(\sigma_m/\sigma_s) \geq \alpha$ is estimated by calculating the minimum of the right-hand side of equation (1) by varying the parameter $R > 1$ numerically. For further details underlying the statistical analysis and the derivation of equation (1), see the supplementary data available from stacks.iop.org/PhysBio/3/45.

Zero-crossing analysis

Zero-crossing analysis (see, for example, [27]) was used to quantitatively analyze the persistence of observed mitochondrial size changes. The FPT analysis of a

hypothetical homogeneously stained fluorescent mitochondrion with constant shape and size will result in normal-distributed size changes (see supplementary figure S1(a)). The probability p that noise in the images will cause an overestimated mitochondrial length (or width) in one image and an underestimated length (or width) in the next (or vice versa) is 50%. The expected average number of such size transitions (herein referred to as zero crossings) for a total of N images is $(N-1)p$ and the probability P for measuring N_0 zero crossings is given by a binomial distribution (see the supplementary data and figure S1(c)). Using the De Moivre–Laplace theorem for $(N-1)p(1-p) \gg 1$, the probability $P^-(N_0)$ for measuring a zero-crossing number smaller than or equal to N_0 is given by (supplementary data)

$$P^-(N_0) = \frac{1}{2} \left[1 - \operatorname{erf} \left(\frac{(N-1)p - N_0}{\sigma\sqrt{2}} \right) \right] = 1 - P^+(N_0), \quad (2)$$

with $P^+(N_0)$ being the probability for measuring any number of zero crossings larger than or equal to N_0 and $\sigma = \sqrt{(N-1)p(1-p)}$ being the standard deviation. Equation (2) was used to determine whether a measured zero-crossing number was significantly decreased or increased compared to the expected mean number of zero crossings for noise-induced size changes.

Supplementary data

Supplementary data, which provides details of calculations, statistical analysis and computer simulations, is available from stacks.iop.org/PhysBio/3/45.

Results

In order to visualize the active transport of mitochondria in living neurons and measure their shapes and sizes, we homogeneously stained mitochondria with the lipophilic cationic dye MitoTracker. To ensure non-invasive CLSM measurements, laser intensity was kept as low as possible while maintaining a sufficient signal-to-noise ratio (SNR) to allow statistically reliable FPT analysis.

Figure 2(a) shows the intensity distribution of an ellipsoidal-shaped dendritic mitochondrion along with the corresponding CLSM image (upper panel). Shown is the first of 100 sequential images. Position, orientation, shape and size of the mitochondrion in each image were obtained by FPT analysis (Materials and methods). The analysis of the first image is shown in figure 2(b). Depicted is the intensity distribution $I_{\text{obj}}(x, y, z = 0)$ of the three-dimensional model object describing the mitochondrion. An x -section through the experimental and theoretical intensity distribution is given in the left inset. The FPT analysis of the image sequence yields the trajectories of the five characteristic object points p_0 to p_4 as indicated in figure 2(c). In figure 2(d), we plotted the traces of the centroid and the rear and the front end of the mitochondrion, $p_0(\tilde{x})$, $p_1(\tilde{x})$ and $p_2(\tilde{x})$, respectively, with respect to the \tilde{x} -axis of the rotated coordinate system \tilde{O} , i.e., with respect to an axis parallel to the major symmetry axis of

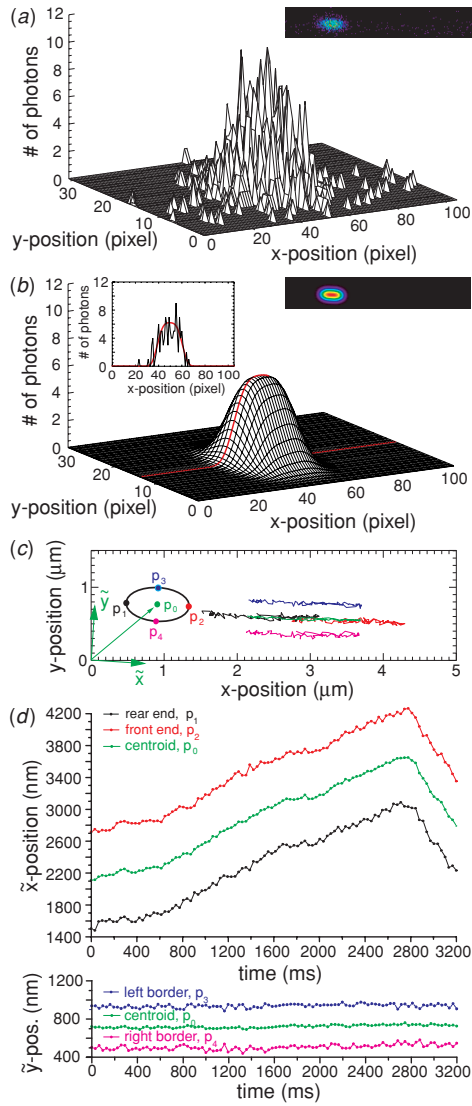


Figure 2. The FPT analysis of an actively transported dendritic mitochondrion. (a) The intensity distribution of the mitochondrion. The graph depicts the left half of the inserted CLSM micrograph (first of 100 sequential images). CLSM image size: 200×32 pixel. Image sampling interval: 32.32 ms. Line scanning time: 1.01 ms. Pixel dwell time: $1.25 \mu\text{s}$. Pixel size: 44 nm (for parameters characterizing the object intensity, see supplementary table S1). (b) Fitted intensity distribution $I_{\text{obj}}(x, y, z = 0)$ of the 3D model object. x -sections along the red line through both the experimental and fitted intensity distributions are shown in the inset. Results of the fit: $p = 10.853$, $d_x = 0$ (fixed), $d_1 = 608$ nm ($d_2 = d_1$, fixed), $d_y = 436$ nm, $I_B = 0.0233$, $\tilde{x}_0 = 48.98$ pixel, $\tilde{y}_0 = 16.2$ pixel and $\varphi = -0.05163$ ($\chi^2 = 1171.5134$). The length of the ellipsoidal-shaped mitochondrion is $d = 1216$ nm. (c) Trajectories of the object points p_0 to p_4 (see inserted schematic). The \tilde{x} -axis of the rotated coordinate system \tilde{O} (green) is aligned with the major symmetry axis of the mitochondrion. The angle of rotation $\varphi = -0.0521$ (corresponds to the direction of transport) is the mean parameter obtained from the FPT analysis of the measured image sequence. (d) Traces of the mitochondrial centroid (p_0) and the front (p_2) and rear (p_1) ends with respect to the \tilde{x} -axis (upper panel). The lower panel depicts the movements of the left (p_3) and right (p_4) mitochondrial borders together with the centroid (p_0) with respect to the \tilde{y} -axis of \tilde{O} .

the mitochondrion (figure 2(c)). The movements of the left and right mitochondrial borders, $p_3(\tilde{y})$ and $p_4(\tilde{y})$, are drawn together with the centroid $p_0(\tilde{y})$ with respect to the \tilde{y} -axis of \tilde{O} (lower part of figure 2(d)). The analysis reveals anterograde movement of $\sim 1.5 \mu\text{m}$ over a period of 2.8 s, followed by a rapid reversal in the retrograde direction (figure 2(d)).

The centroid movement can be ‘linearized’ by trace sectioning and fitting straight lines to the resulting trace segments (figure 3(a)). The mitochondrion is transported in a linear fashion with various mean velocities during continuous unidirectional movement, except for a few small deviations from the fitted lines. While the traces of the mitochondrial front (p_2) and rear (p_1) ends reflect on average similar linear movements (figure 2(d)), the deviations of the latter seem to be markedly higher than those observed for the centroid. To visualize these deviations, we superimposed the traces of the front and rear ends by subtracting the measured mean mitochondrial length from the front-end trace shown in figure 2(d) and then plotted the distance traveled by both ends after applying a three-point moving window (figure 3(b)).

The superimposed traces reveal non-simultaneous displacements of both mitochondrial ends. To help visualize these features, we shifted the front-end trace depicted in figure 3(b) toward the origin of the coordinate system (figure 3(c)). Interestingly, the rear end seems to start in the lead and to dictate the movement in the anterograde direction. The front end apparently lags behind. While the rear end is displaced by ~ 100 nm between the second and third images (step 1, figure 3(c)), the front end is lagging. The displacement of the rear end is then followed by an immobile period; ~ 140 ms after the initial displacement of the rear end, the front end seems to catch up and makes a move over the same distance of ~ 100 nm (step 2, figure 3(c)). The alternating non-simultaneous mobile and immobile periods of both ends result in mitochondrial length changes as illustrated in the inset of figure 3(c). A pause of movement of both ends is then again followed by a displacement of the rear end first (step 3, figure 3(c)). Following a displacement of ~ 650 nm in the anterograde direction the rear end pauses for a while, and then moves forward (step 4, figure 3(c)). A similar pause is made ~ 90 ms later by the front end (step 5, figure 3(c)). After a distance of ~ 1550 nm, the rear end seems to introduce the backward movement while the front end still moves forward resulting in simultaneously opposing displacements of both ends (step 6, figure 3(c) and gray-shaded rectangle in figure 3(b)). In sum, both mitochondrial ends undergo similar characteristic movements with substantial time delay between the displacements of both ends (see arrows in figure 3(c)). To visualize the similarity of the movements of both ends, we superimposed trace segments in figure 3(b) and indicated the approximate time delay.

The validity of the above interpretation depends on the precision of the measurement. Noise in the images could potentially be a source for some of the observations made. Hence, we simulated the movements of a mitochondrion of the same shape and size as the experimental mitochondrion and being transported with identical mean velocities (figure 3(a)) whereas the shape and size parameters were kept

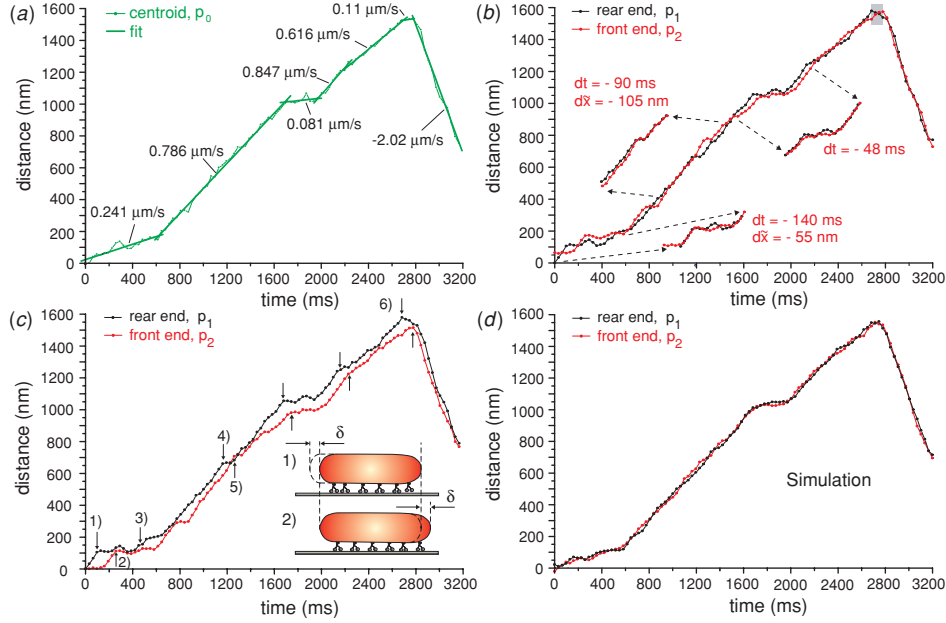


Figure 3. Displacement traces of the mitochondrial front and rear ends of experiment (see figure 2) and simulation. (a) Displacement of the centroid (p_0) along the \tilde{x} -axis of \tilde{O} . The superimposed straight lines depict the result of the fits to the various trace sections (see the main text). (b) Superimposed smoothed displacement traces (with respect to the \tilde{x} -axis) of the mitochondrial front and rear ends. The superposition of the traces was achieved in two steps. First, the measured mean mitochondrial length of $\bar{d} = 1178.4$ nm was subtracted from the front end trace (p_2) shown in the upper panel of figure 2(d) and second, the \tilde{x} -position of the rear end (p_1) in the first image was subtracted from both the resulting trace and the trace of the rear end. Finally, we applied a three-point moving window. The inserted trace segments (see dashed arrows) were superimposed by shifting the corresponding segments of the front end trace along the time- and \tilde{x} -axis by the indicated values dt and $d\tilde{x}$, respectively. The gray-shaded rectangle marks simultaneously opposing displacements of both mitochondrial ends. (c) Front and rear end traces after moving the front end trace shown in (b) of this figure by 60 nm toward the origin of the \tilde{x} -axis. The inserted schematic illustrates the length changes of the mitochondrion during the first 300 ms of the measurement. (d) Smoothed displacement traces of the simulated mitochondrion (a detailed description of the simulation is provided in the supplementary data and figure S2).

constant (figure 3(d)) (for more details, see the supplementary data and figure S2). Significantly, these traces do not exhibit the substantial time-delayed displacements between both mitochondrial ends that we see in the experiment.

Statistical analysis of the standard deviations of the mitochondrial length d and width d_y taken from the experiment ($\sigma_d = 48.6$ nm and $\sigma_{d_y} = 34.4$ nm) and the simulation ($\sigma_d = 33.5$ nm and $\sigma_{d_y} = 30.1$ nm) reveals a significantly increased standard deviation for the mitochondrial length ($P < 0.009$, equation (1)), whereas the standard deviations for the experimental and simulated mitochondrial width were statistically indistinguishable ($P < 0.36$) (see the supplementary data available from stacks.iop.org/PhysBio/3/45 for more details).

Next, we examined the mitochondrial size changes observed, using the zero-crossing analysis (Materials and methods). The expected mean number of zero crossings (size transitions) for a total of 100 images is 49.5. The experiment results in 37 ($P^- < 0.006$, equation (2)) and 45 ($P^- < 0.18$) zero crossings for the length and width, respectively, demonstrating a significantly decreased number of zero crossings along the direction of transport (see also supplementary figure S1(c)). In contrast, both zero-crossing numbers gained from the simulation are close to the expectation (52, $P^+ < 0.31$, equation (2)). This strongly

suggests systematic length changes of the measured mitochondrion, a result in agreement with the observed time-delayed movements of the mitochondrial ends.

Figure 4 shows an example of an apparently immobile mitochondrion together with a mobile mitochondrion (a detailed analysis of an oscillating forward and backward moving mitochondrion is provided in the supplementary data, see figure S4). Figure 4(a) depicts the intensity distributions together with the CLSM micrograph of both mitochondria. Shown is the first image of 90 sequential images. The trajectories of the object points p_0 to p_4 (see the inset of figure 4(c)) are shown in figure 4(b). The mitochondrion on the right-hand side moves toward the center of the image in the retrograde direction while the mitochondrion on the left-hand side appears to be immobile. The displacement traces of the front and rear ends of both mitochondria after applying a three-point moving window are shown in figures 4(c) and (d) (the original data traces are shown in supplementary figures S3(a) and (b)). Similar to the example shown in figure 3(a), transport of the mobile mitochondrion appears to be accomplished in a linear fashion with sections of different mean velocities during continuous unidirectional movement (inset, figure 4(e)). Both mitochondria seem to undergo persistent length and width changes (figures 4(c) and (d)). Here, zero-crossing analysis results in 32 ($P^- < 0.004$) and

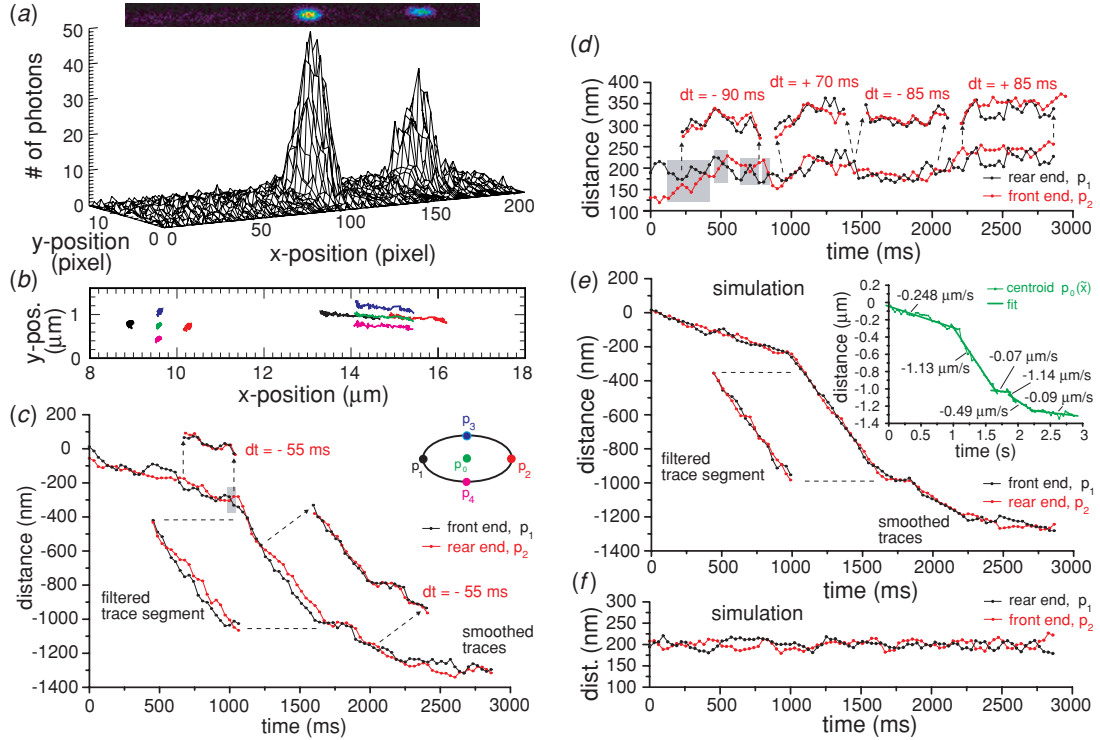


Figure 4. Simultaneous measurement of an apparently immobile and mobile dendritic mitochondrion. (a) Intensity distributions of both mitochondria in the first of 90 sequential images (the corresponding CLSM micrograph is shown in the inset). CLSM image size: 208×16 pixel. Image sampling interval: 32.16 ms. Line scanning time: 2.01 ms. Pixel dwell time: $5.15 \mu\text{s}$. Pixel size: 88 nm (for parameters characterizing the object intensities, see supplementary table S2). (b) Trajectories of the object points p_0 to p_4 of both mitochondria (see inserted schematic in (c) of this figure). (c) Displacement traces (with respect to an axis parallel to the major mitochondrial symmetry axis) of the front and rear ends of the mobile mitochondrion after applying a three-point moving window to the original traces shown in supplementary figure S3(a) (mean transport direction: $\varphi = -0.0398 \pm 0.0215$). The inserted trace segment on the left-hand side depicts a characteristic part of the mitochondrial displacement traces after applying a 0.01 Hz low-pass filter to the original traces (the dashed lines mark the corresponding part of the smoothed traces). The inserted trace segments (see dashed arrows) were superimposed by shifting the corresponding parts of the front end trace by -55 ms in time. (d) Smoothed displacement traces of the apparently immobile mitochondrion (the original traces are shown in supplementary figure S3(b)) (mean object orientation: $\varphi = -0.0486 \pm 0.0317$). The insets show superimposed trace segments of the mitochondrial front and rear ends (dt indicates the corresponding time delays). (e) Smoothed displacement traces of the front and rear ends of the simulated mobile mitochondrion (see supplementary data for a detailed description of the underlying simulation). The inserted trace segment depicts a low-pass-filtered part of the original traces shown in supplementary figure S3(c). The graph above the smoothed traces shows the original displacement trace of the centroid (p_0) (with respect to an axis parallel to the major mitochondrial symmetry axis) of the measured mobile mitochondrion. The superimposed straight lines depict the result of the fits to the various trace sections. (f) Smoothed displacement traces of the front and rear ends of the simulated immobile mitochondrion (see supplementary data and figure S3(d) for more information).

39 ($P^- < 0.12$) zero crossings for the length and width of the mobile mitochondrion (the expected mean number of zero crossings for 90 images is 44.5) and in 41 ($P^- < 0.23$) and 43 ($P^- < 0.38$) zero crossings for the length and width of the immobile mitochondrion, respectively. The persistence of size changes is thus statistically validated only for the length changes of the mobile mitochondrion.

The traces of the mobile mitochondrion again reveal similar time-delayed displacements of both ends (figure 4(c)). To help visualize characteristic features present in the original data traces (supplementary figure S3(a)), we applied a 0.01 Hz low-pass filter and inserted a segment of the resulting traces (inset, figure 4(c)). Apparently, the front end dictates movement and the rear end lags behind, a feature reminiscent of an inchworm-like motility mechanism. The simulated mitochondrion, on the other hand, does not exhibit such

a characteristic feature (see the filtered trace segment in figure 4(e)). Within this segment, the measured non-averaged traces do not cross each other for 14 sampling intervals (supplementary figure S3(a)). The probability for such an event is 0.005 (see the supplementary data available from stacks.iop.org/PhysBio/3/45). This result clearly indicates systematic mitochondrial length changes over the entire duration of the depicted trace segment (figure 4(c)).

Mitochondrial length changes and the similarity of the time-delayed displacements of both mitochondrial ends appear to be a typical feature of mitochondria transport: For a proof-of-principle, we took 25 measurements of actively transported mitochondria (all from dendrites of different neurons) from which eight measurements met the described criteria for reliable FPT analysis (see section ‘finite-particle tracking (FPT) analysis’) and provided a sufficient SNR (the remainders were discarded due to extensive photobleaching and/or the

release of the accumulated dye during image acquisition and/or a poor mitochondrial uptake of the fluorescent dye). All eight measurements revealed statistical significant mitochondrial length fluctuations (judged by SD analysis). Although all traces also showed segments of apparent time-delayed similar displacements (see, e.g., supplementary figure S4), only four experiments provided a sufficiently high tracking precision to allow their validation via comparison with simulated traces (see figures 3 and 4 and supplementary figure S5), demonstrating the need for a significantly increased SNR using a different staining strategy (see Discussion).

The inserted superimposed trace segments in figures 4(c) and (d) demonstrate once again the similarity of the movements of both ends (Δt indicates the approximate time delay). Such substantial time-delayed movements are absent in simulated traces (figures 4(e) and (f), see also supplementary figure S3). Importantly, the rear end of the mobile mitochondrion (figure 4(c)) always lags behind the front end, whereas the front and rear ends of the immobile mitochondrion (figure 4(d)) apparently switch leading and lagging roles (alternating negative and positive time delays of ~ 80 ms). Moreover, the front and rear ends of the immobile mitochondrion seem to undergo substantial simultaneously opposing displacements during the first 800 ms of data acquisition (see, gray-shaded rectangles in figure 4(d)), suggestive for a tug-of-war between both ends. This interpretation is supported by the almost identical time-delayed displacements of both ends (see inserted superimposed trace segments on the left-hand side of figure 4(d)), by the comparison with the simulated traces (figure 4(f)) and the statistically validated length changes of this mitochondrion (see above). The apparently immobile mitochondrion does, thus, appear to exhibit substantial size changes presumably due to competitive activity at both mitochondrial ends. Collectively, our data clearly show that mitochondria undergo characteristic size changes during movement.

Discussion

We have applied a recently developed FPT algorithm [24] and analyzed mitochondria transport in dendrites of cultured neurons. Quantitative analysis of the data obtained revealed transport-induced submicroscopic-size changes of mitochondria. Front and rear ends of mitochondria can undergo similar characteristic movements with substantial time delay between the displacements of both ends, an observation reminiscent of inchworm-like locomotion. Furthermore, we have demonstrated that both mitochondrial ends can play distinctive roles during transport—while one of the ends leads, the other lags behind. Both the observed alternating leading roles and the detected simultaneously opposing displacements of the mitochondrial ends could suggest an occasional tug-of-war between both ends.

To quantitatively analyze shape and size changes of mitochondria, we have explicitly taken into account the noise-limited localization precision of object borders and simulated fluorescence images of mitochondria by adopting the object parameters and noise characteristics of a given

experiment. By performing statistical and zero-crossing analysis of experimental and simulated data, we have shown that processively transported mitochondria can undergo persistent submicroscopic-length changes. As the direction of length changes coincides with the direction of transport, our investigation suggests the length changes to be transport related. Mitochondrial length changes were in part brought about by non-simultaneous displacements of both ends. As the time-delayed movements of either cargo ends had the same mean velocity (identical shape and curvature of the smoothed trace segments, see figures 3(b) and 4(c)), we propose these movements to be motor-driven rather than being caused by elastic forces that could potentially lead to some type of ‘oscillatory’ or ‘jumping’ motion of the lagging end.

Several processes could potentially cause shape and size changes of the cargo (motion blur caused by the line-scanning process of the laser scanning microscope can be neglected, see the supplementary data available from stacks.iop.org/PhysBio/3/45). (i) unsynchronized activity of motor proteins attached to the front and rear ends of the cargo could potentially cause size changes, (ii) obstacles in the relatively crowded intracellular environment could hamper simultaneous movement of both cargo ends and (iii) switching between the end of one microtubule to the beginning of the next might interfere with simultaneous displacements of both cargo ends. However, those processes are unlikely to account for the observed time-delayed similar movements of both cargo ends (e.g., direction reversals or movement with a certain speed followed by a characteristic pause, see figures 3(b) and 4(c) and (d)). The finding that the time-delayed movements of the leading and trailing mitochondrial ends were almost identical (see above) and that they occurred at spatially different positions in the dendrite (more than $1\ \mu\text{m}$ apart in the presented examples, see figure 2(d)) rather suggests that the (motor) activity at one end is somehow communicated to the other end. What signal could spread along the length of a mitochondrion in about 50–150 ms (see figures 3 and 4)? Signal pathways could potentially involve forces exerted along the cargo membrane. Although forces that activate/deactivate or modulate motor function via strain-sensitive motor-cofactor proteins cannot be yet ruled out, they are expected to take effect in a time much faster than the measured time delay of tens of milliseconds [28]. In a different scenario, forces could act directly on motor proteins and cause motor stalling or even make them moving backward [29] (for a detailed discussion on a tug-of-war between motor proteins, see the supplementary data available from stacks.iop.org/PhysBio/3/45) though such a mechanism (when continuously utilized) seems to be too inefficient from the energetic point of view and not supported by the current state of research [8]. A principally different pathway, on the other hand, could involve waves of signal molecules that propagate along the cargo membrane. Given a mitochondrial length of about $1.3\ \mu\text{m}$ (see examples in figures 2 and 4), this signal must travel with a speed in the range of $9\text{--}26\ \mu\text{m s}^{-1}$. Thus, waves of second messengers such as Ca^{2+} or cyclic adenosine 3',5'-monophosphate (cAMP) would be good candidates as these waves are known to

travel over long distances across the cell with a speed in the range of 8–100 $\mu\text{m s}^{-1}$ [30] and are likely involved in the regulation of bidirectional organelle transport via $[\text{Ca}^{2+}]$ - and $[\text{cAMP}]$ -dependent phosphorylation/dephosphorylation of motor proteins [21–23, 31, 32]. In particular, the speed of Ca^{2+} waves in astrocytes and neurites of PC12 cells and neurons has been determined to be in the range of 5–30 $\mu\text{m s}^{-1}$ [33, 34], 17–30 $\mu\text{m s}^{-1}$ [35] and 10 $\mu\text{m s}^{-1}$ [36], respectively, in good agreement with the anticipated velocity range. Besides $[\text{Ca}^{2+}]$ -sensitive phosphorylation/dephosphorylation of motor proteins, $[\text{Ca}^{2+}]$ -dependent motor regulation by calmodulin might play a role [37, 38]. Taken together, the detected time-delayed movements of both mitochondrial ends might provide new hints for the mechanism underlying bidirectional organelle transport.

The observed simultaneously opposing displacements of the leading and trailing ends of mitochondria could in particular indicate an occasional tug-of-war between opposite-polarity motor proteins or motor proteins of the same directionality but moving along anti-parallel microtubules since microtubules are of mixed orientation in proximal dendrites [39, 40]. Whereas an occasional tug-of-war between motors of the same type that carries a mitochondrion through a network of anti-parallel microtubules is not an unexpected scenario [7], competitive activity of opposite-polarity motors in processes with uniform aligned microtubules is controversial [8]. In fact, a recent high-precision single-particle tracking (SPT) study on actively transported GFP-tagged peroxisomes in S2 cells [28] strongly argues against a tug-of-war scenario in such processes. However, as is typical for studies that provide indirect evidence for a proposed mechanism, the same data can be interpreted in favor of a model partially based on a tug-of-war between motor molecules (see the supplementary data available from stacks.iop.org/PhysBio/3/45), demonstrating the need for direct evidence for the underlying mechanism of bidirectional organelle transport.

To prove that our observations are of a general nature and not restricted to mitochondria transport in proximal dendrites, transport in distal dendrites [39, 40] or axonal transport has to be analyzed. However, a thorough study of the reported processes in dendrites and axons that does not require extensive computer simulations awaits both an improved tracking precision and an increased time resolution. The low excitation intensity and small pixel dwell time (to prevent photodamage of mitochondria), the photodetector deadtime and the use of an exogenous dye for the staining of mitochondria prevented us from achieving tracking precisions in the lower nanometer range [24]. Despite the modest tracking precision, we were able to gain statistically validated information about mitochondrial size changes using computer simulations.

Conclusion and outlook

Our study unequivocally revealed transport-induced submicroscopic-size changes of mitochondria and thus demonstrated the potential impact of shape and size analysis

of actively transported finite objects. In combination with an improved time resolution, an increased tracking precision and the use of RNAi analysis (RNAi has not yet been undertaken in neurons from *Xenopus laevis*; therefore, other neuronal cell systems such as cultured rat sympathetic neurons could be tried out, see [41]) the provided biophysical framework will prove to be an excellent tool for studying the mechanism of bidirectional organelle transport in living cells. Deciphering the source of the observed simultaneously opposing displacements and the time-delayed similar movements of both mitochondrial ends and the potential simultaneous detection of opposing motor steps could have profound implications for the mechanism underlying bidirectional organelle transport.

Acknowledgments

The authors wish to thank N O Petersen for stimulating and invaluable discussions and C Wald and B Beyerstedt for help with statistical analysis. This work has been supported by DFG Research Center of Molecular Physiology of the Brain (DS), DFG grant GE 1609/1 (AG), and BCCN grant 01GQ0432 (DS).

Glossary

Tug-of-war. Motor proteins pulling against each other.

Zero crossings. Commonly defined as the number of times a signal crosses the zero level, with either a positive or negative slope. Here it is defined as the number of times a mitochondrion changes its length (or width, respectively) between images from a value larger than the measured mean length (or width) to a value smaller than the measured mean length (or width) or vice versa.

Finite-particle tracking (FPT). Localization and tracking of a finite-sized fluorescent object in subsequent images. The size and shape of the three-dimensional object are taken into account by the FPT algorithm, in contrast to a SPT algorithm in which the object (commonly a fluorescent molecule) is assumed to be a point object.

Anterograde transport. Movement toward the synapse.

Retrograde transport. Movement toward the cell body.

References

- [1] Hollenbeck P J 1996 The pattern and mechanism of mitochondrial transport in axons *Front. Biosci.* **1** d91–120
- [2] Brady S T 1991 Molecular motors in the nervous system *Neuron* **7** 521–33
- [3] Hirokawa N 1998 Kinesin and dynein superfamily proteins and the mechanism of organelle transport *Science* **279** 519–26
- [4] Vale R D 2003 The molecular motor toolbox for intracellular transport *Cell* **112** 467–80
- [5] Hirokawa N and Takemura R 2005 Molecular motors and mechanisms of directional transport in neurons *Nat. Rev. Neurosci.* **6** 201–14
- [6] Schliwa M 2003 *Molecular Motors* (Germany: VCH-Wiley)
- [7] Welte M A 2004 Bidirectional transport along microtubules *Curr. Biol.* **14** R525–37

- [8] Gross S P 2004 Hither and Yon: a review of bi-directional microtubule-based transport *Phys. Biol.* **1** R1–11
- [9] Hirokawa N, Sato-Yoshitake R, Yoshida T and Kawashima T 1990 Brain dynein (MAP1C) localizes on both anterogradely and retrogradely transported membranous organelles *in vivo* *J. Cell Biol.* **111** 1027–37
- [10] Ma S and Chisholm R L 2002 Cytoplasmic dynein-associated structures move bidirectionally *in vivo* *J. Cell Sci.* **115** 1453–60
- [11] Gross S P, Tuma M C, Deacon S W, Serpinskaya A S, Reilein A R and Gelfand V I 2002 Interactions and regulation of molecular motors in *Xenopus Melanophores* *J. Cell Biol.* **156** 855–65
- [12] Gross S P, Guo Y, Martinez J E and Welte M A 2003 A determinant for directionality of organelle transport in *Drosophila* embryos *Curr. Biol.* **13** 1660–8
- [13] De Vos K J, Sable J, Miller K E and Sheetz M P 2003 Expression of phosphatidylinositol (4,5) bisphosphate-specific pleckstrin homology domains alters direction but not the level of axonal transport of mitochondria *Mol. Biol. Cell* **14** 3636–49
- [14] Ligon L A, Tokito M, Finklestein J M, Grossman F E and Holzbaur E L 2004 A direct interaction between cytoplasmic dynein and kinesin I may coordinate motor activity *J. Biol. Chem.* **279** 19201–08
- [15] Gross S P, Welte M A, Block S M and Wieschaus E F 2002 Coordination of opposite-polarity microtubule motors *J. Cell Biol.* **156** 715–24
- [16] Waterman-Storer C M, Karki S B, Kuznetsov S A, Tabb J S, Weiss D G, Langford G M and Holzbaur E L 1997 The interaction between cytoplasmic dynein and dynactin is required for fast axonal transport *Proc. Natl Acad. Sci. USA* **94** 12180–5
- [17] Martin M, Iyadurai S J, Gassman A, Gindhart J G Jr, Hays T S and Saxton W M 1999 Cytoplasmic dynein, the dynactin complex, and kinesin are interdependent and essential for fast axonal transport *Mol. Biol. Cell* **10** 3717–28
- [18] Valetti C, Wetzel D M, Schrader M, Hasbani M J, Gill S R, Kreis T E and Schroer T A 1999 Role of dynactin in endocytic traffic: effects of dynamitin overexpression and colocalization with CLIP-170 *Mol. Biol. Cell* **10** 4107–20
- [19] Deacon S W, Serpinskaya A S, Vaughan P S, Lopez Fanarraga M, Vernos I, Vaughan K T and Gelfand V I 2003 Dynactin is required for bidirectional organelle transport *J. Cell Biol.* **160** 297–301
- [20] Welte M A, Gross S P, Postner M, Block S M and Wieschaus E F 1998 Developmental regulation of vesicle transport in *Drosophila* embryos: forces and kinetics *Cell* **92** 547–57
- [21] Sato-Yoshitake R, Yorifuji H, Inagaki M and Hirokawa N 1992 The phosphorylation of kinesin regulates its binding to synaptic vesicles *J. Biol. Chem.* **267** 23930–6
- [22] Dillman J F III and Pfister K K 1994 Differential phosphorylation *in vivo* of cytoplasmic dynein associated with anterogradely moving organelles *J. Cell Biol.* **127** 1671–81
- [23] Lee K D and Hollenbeck P J 1995 Phosphorylation of kinesin *in vivo* correlates with organelle association and neurite outgrowth *J. Biol. Chem.* **270** 5600–05
- [24] Gennerich A and Schild D 2005 Sizing-up finite fluorescent particles with nanometer-scale precision by convolution and correlation image analysis *Eur. Biophys. J.* **34** 181–99
- [25] Bischofberger J and Schild D 1995 Different spatial patterns of $[Ca^{2+}]$ increase caused by N- and L-type Ca^{2+} channel activation in frog olfactory bulb neurons *J. Physiol.* **487** 305–17
- [26] Gennerich A and Schild D 2000 Fluorescence correlation spectroscopy in small cytosolic compartments depends critically on the diffusion model used *Biophys. J.* **79** 3294–306
- [27] Papoulis A and Pillai S U 2002 *Probability, Random Variables, and Stochastic Processes* 4th edn (New York: McGraw-Hill)
- [28] Kural C, Kim H, Syed S, Goshima G, Gelfand V I and Selvin P R 2005 Kinesin and dynein move a peroxisome *in vivo*: a tug-of-war or coordinated movement? *Science* **308** 1469–72
- [29] Carter N J and Cross R A 2005 Mechanics of the kinesin step *Nature* **435** 308–12
- [30] Meyer T 1991 Cell signaling by second messenger waves *Cell* **64** 675–8
- [31] Donelan M J *et al* 2002 Ca^{2+} -dependent dephosphorylation of kinesin heavy chain on β -granules in pancreatic β -cells *J. Biol. Chem.* **277** 24232–42
- [32] Hollenbeck P J 1993 Phosphorylation of neuronal kinesin heavy and light chains *in vivo* *J. Neurochem.* **60** 2265–75
- [33] Charles A C and Giaume C 2002 *The Tripartite Synapse* ed A Volterra, P J Magistretti and P G Haydon (New York: Oxford University Press) pp 110–26
- [34] Bernardinelli Y, Magistretti P J and Chatton J Y 2004 Astrocytes generate Na^{+} -mediated metabolic waves *Proc. Natl Acad. Sci. USA* **101** 14937–42
- [35] Lorenzon P, Zacchetti D, Codazzi F, Fumagalli G, Meldolesi J and Grohovaz F 1995 Ca^{2+} waves in PC12 neurites: a bidirectional, receptor-oriented form of Ca^{2+} signaling *J. Cell Biol.* **129** 797–804
- [36] Ennes H S, Young S H, Raybould H E and Mayer E A 1997 Intercellular communication between dorsal root ganglion cells and colonic smooth muscle cells *in vitro* *NeuroReport* **8** 733–7
- [37] Hisanaga S and Sakai H 1983 Cytoplasmic dynein of the sea urchin egg: II. Purification, characterization and interactions with microtubules and Ca-calmodulin *J. Biochem. (Tokyo)* **93** 87–98
- [38] Hisanaga S and Pratt M M 1984 Calmodulin interaction with cytoplasmic and flagellar dynein: calcium-dependent binding and stimulation of adenosinetriphosphatase activity *Biochemistry* **23** 3032–7
- [39] Burton P R 1988 Dendrites of mitral cell neurons contain microtubules of opposite polarity *Brain Res.* **473** 107–15
- [40] Baas P W, Deitch J S, Black M M and Banker G A 1988 Polarity orientation of microtubules in hippocampal neurons: uniformity in the axon and nonuniformity in the dendrite *Proc. Natl Acad. Sci. USA* **85** 8335–9
- [41] He Y, Francis F, Myers K A, Yu W, Black M M and Baas P W 2005 Role of cytoplasmic dynein in the axonal transport of microtubules and neurofilaments *J. Cell Biol.* **168** 697–703

Supplementary data

Cell culture

Cultured neurons of the olfactory bulb of *Xenopus laevis* tadpoles were prepared as described by Bischofberger and Schild [1]. Briefly, larvae of *X. laevis* (stage 48 to 54, [2]) were anesthetized with Tricain (100 mg/l), and the olfactory bulbs were extirpated. The tissue was incubated at 22°C for 90 min in a dissociation solution containing EDTA (1 mM), papain (30 U/ml), and cysteine (1.5 mM). The resulting pieces were triturated with an Eppendorf pipette. The cells were plated onto dishes coated with poly-L-lysine (50 µg/ml) and laminin (20 µg/ml) in a drop of medium (50 µl) containing 70% L15, 10% horse serum, and 50 µg/ml gentamycin. After 20 h, 0.1 ml of growth medium, which contained 75% L15, 5% horse serum, and 59 µg/ml gentamycin, was added, allowing the cells to condition their own environment. Measurements were carried out within two weeks of the plating.

The cultured cells were characterized with the use of antibodies against glial cells and GABAergic neurons. Mitral cells were identified by injection of fluorescent beads into the lateral olfactory tract and successive retrograde labeling [1]. Mitral cells appeared as the largest neurons in the culture and were multipolar, whereas glutamic acid decarboxylase-positive cells were smaller and of ellipsoidal shape. Prior to the CLSM measurements, the culture medium was replaced by the following bath solution: 98 mM NaCl, 2 mM KCl, 2 mM MgCl₂, 1 mM CaCl₂, 5 mM Glucose, 5 mM NaPyruvat, 10 mM HEPES, 225 mOsm, pH 7.8.

Staining of mitochondria

Mitochondria were labeled with the fluorescent dye MitoTracker Orange CMTRos (Molecular Probes, Leiden, The Netherlands), a lipophilic cationic dye derived from Tetramethylrosamin for staining of living mitochondria. Prior to the CLSM measurements, the cultured neurons were incubated for ~10 min in 10 nM Mito-Tracker dissolved in the bath solution. MitoTracker accumulated preferentially in mitochondria due to their negative transmembrane potential. Measurements were performed after rinsing of the bath. As well as its use as a fluorescence marker, MitoTracker also served as a marker of metabolic mitochondrial activity during image acquisition. A decrease in the mitochondrial potential (e. g., due to a loss of activity caused by light exposure, [3]) results in a release of the accumulated fluorophore. Hence, laser intensity and pixel dwell time were kept as low as necessary to ensure non-invasive measurements.

Computer simulations

Sequences of fluorescence images of both stationary and linearly transported mitochondria (see below) were simulated by adding normal-distributed noise [4] to the theoretical noise-free intensity distribution $I_{obj,I_B}(x_i, y_i) = I_{obj}(x_i, y_i) + I_B$ describing the model object including the mean background intensity I_B (see also the first paragraph of the section ‘Statistical analysis based on data from two processes’ in the main text). The experimental and simulated images have the same image and pixel size, photon counting characteristics per pixel (see below and the inset of figure S2(a)), mean background intensity, standard deviation σ_{sig} of the object intensity distribution [4] and mean maximum signal above background I_0 . The noise simulation takes explicitly into account the deadline-affected photon detection [4]. The intensity values at (x_i, y_i) were generated either from a Poisson distribution with mean intensity $I_{obj,I_B}(x_i, y_i)$ (in which case $I_{obj,I_B}(x_i, y_i) \leq 1.5 \text{ Mcps}$) or from a Gaussian distribution (in which case $I_{obj,I_B}(x_i, y_i) > 1.5 \text{ Mcps}$). The standard deviation σ of the Gaussian distribution with mean $I_{obj,I_B}(x_i, y_i)$ was calculated according to the fourth order polynomial describing the variance σ^2 of an intensity signal as a function of the mean intensity as described previously (see the caption of figure 1 in [4]). Accordingly, the noise characteristics of the simulated and the measured images were the same.

The intensity distribution $I_{obj}(x_i, y_i)$ of the model object was calculated using the object size parameters of the experimental mitochondrion (\bar{d}_1 , \bar{d}_2 , \bar{d}_x and \bar{d}_y , respectively, see the section ‘Materials and methods’ in the main text) and the average angle $\bar{\varphi}$ by which the mitochondrion was oriented with respect to the x -axis of the coordinate system O . The underlying model object had thus, on average, the same shape, size and orientation as the experimental mitochondrion. In order to analyze the effect of noise on mitochondrial size changes, shape and size of the model object were kept constant over

subsequent images. Linear mitochondrion transport was simulated by displacing the position $p_0 = (x_0, y_0)$ of the model object with sub-pixel precision from image to image along the \tilde{x} -axis of the rotated coordinate system \tilde{O} according to the distances calculated from the mean transport velocities and image acquisition time given by the underlying experiment. The object position of the first image was set to the position of the mitochondrion in the first experimental image. To simulate an immobile mitochondrion, its position was kept constant and set to the mean position $\bar{p}_0 = (\bar{x}_0, \bar{y}_0)$ of the experimental mitochondrion.

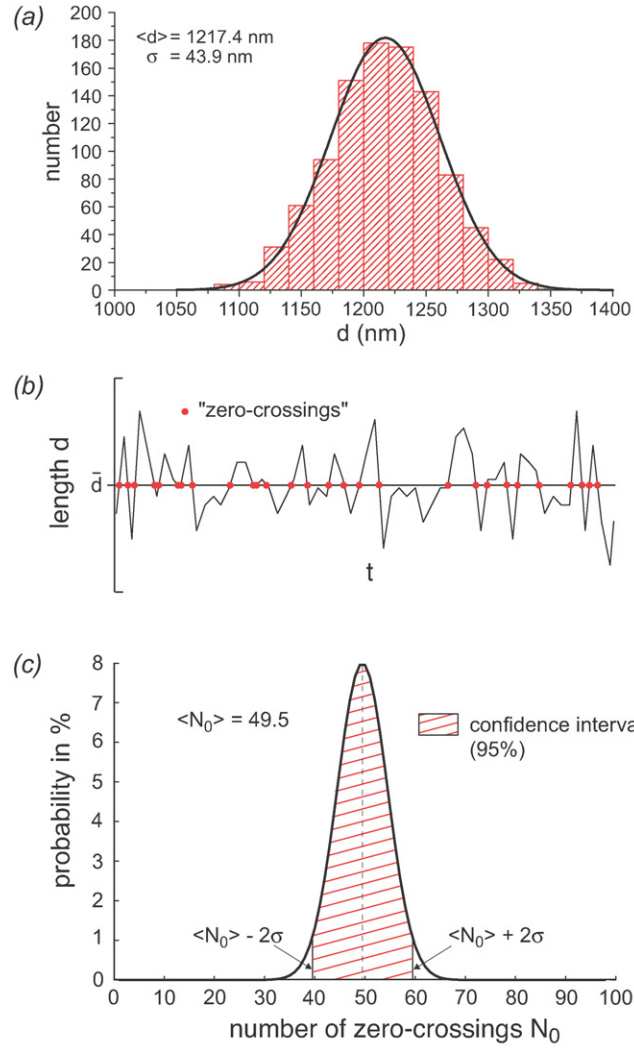


Figure S1. Statistics of mitochondrial length fluctuations. (a) Histogram of the measured length d of a simulated mitochondrion and its fit to a Gaussian function ($r = 0.9984$). Shown is the result of the FPT analysis of 1000 simulated images. The parameters underlying the simulation are the mean parameters obtained from the FPT experiment shown in figure S4. The position of the object was fixed for all images and located in the center of the image ($134 \times 16 \text{ pixel}$). (b) Illustration of the normal distributed mitochondrial length as a function of time. Filled red circles depict the transitions ('zero crossings') from a length d larger than the measured mean length \bar{d} to a length smaller than the mean length and *vice versa*. (c) Binomial probability distribution (equation (S15)) as a function of the number of zero-crossings N_0 ($p = 0.5$, $N = 100$).

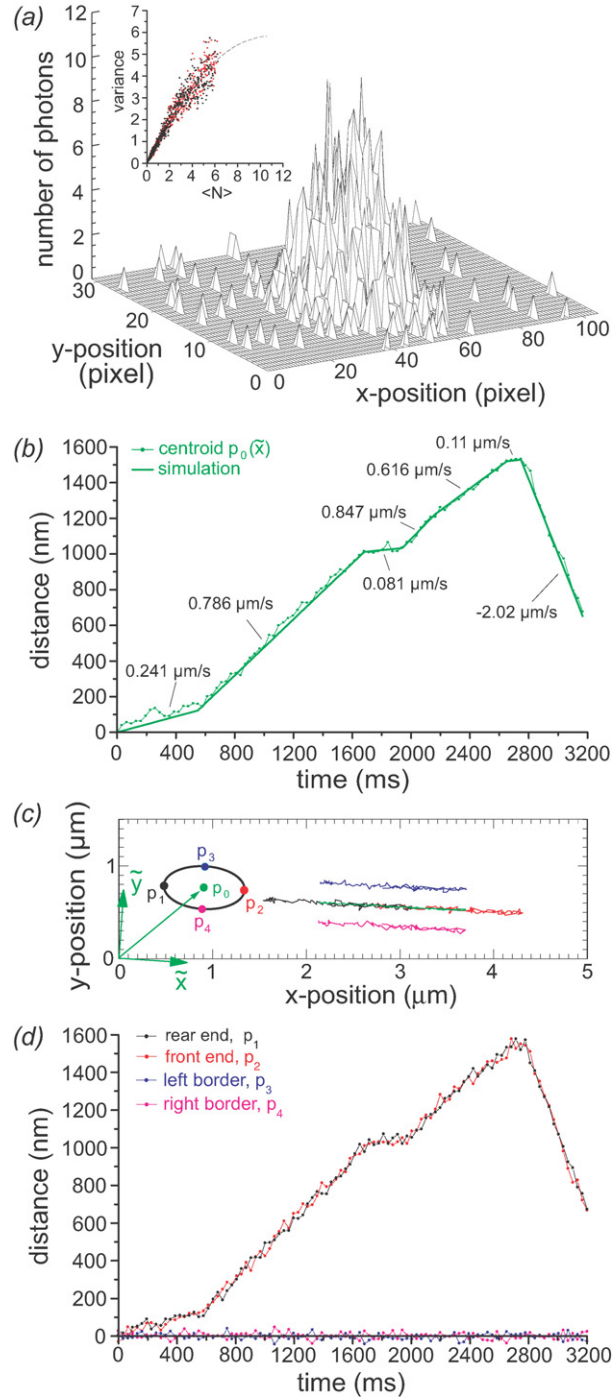


Figure S2. FPT analysis of a simulated linear transported mitochondrion (simulation accompanying the experimental example shown in figure 2 of the main text). (a) Simulated mitochondrion intensity distribution of the first of 100 images (the graph depicts the left half of the CLSM image of 200×32 pixel). Image sampling interval: 32.32 ms. Line scanning time: 1.01 ms. Pixel dwell time: 1.25 μs . Pixel size: 44 nm. The inset depicts the variance (in # of photons) of the photon counting number N as a function of the measured mean number $\langle N \rangle$ (in # of photons) for both the simulated images (filled red circles) and experimental images (filled black circles). Data values were obtained in two

steps: First, object intensity distributions in all images were shifted to the image center (to ensure the alignment of the intensity distributions in the subsequent images). The necessary displacements in x - and y -direction were calculated from the object center $p_0 = (x_0, y_0)$ obtained from FPT analysis of each image. Second, for each pixel that belonged to the set $M_{obj} = \{(i, j) \in x \times y \mid \bar{I}_{obj} \geq 10^{-2} \times I_0\}$ and thus contained an object intensity value [4], the mean and variance of the intensity values in all sequential images of that pixel were calculated. (b) Displacement of the centroid (p_0) of the experimental mitochondrion (see also figure 3(a) in the main text) along the \tilde{x} -axis of \tilde{O} . The superimposed straight lines depict the movement of the simulated mitochondrion. The parameters underlying the simulation were the mean parameters obtained from the FPT analysis of the measured image sequence (mean \pm SD): $p = 10.7 \pm 1.7$, $d_x = 0$ (fixed), $d = d_1 + d_2 = (1178 \pm 49)\text{nm}$ ($d_1 = d_2$), $d_y = (431 \pm 35)\text{nm}$, $I_B = 0.025 \pm 0.005$, and $\varphi = -0.0521 \pm 0.0374$. (c) Trajectories of the characteristic object points p_0 to p_4 (see inset for the color key). The \tilde{x} -axis of the rotated coordinate system \tilde{O} (green) is aligned with the major symmetry axis of the mitochondrion. (d) Displacement traces of the mitochondrial front (red trace) and rear (black trace) ends with respect to the \tilde{x} -axis and the left (blue trace) and right (magenta trace) mitochondrial borders with respect to the \tilde{y} -axis of \tilde{O} obtained from the FPT analysis of the simulated image sequence.

Statistical analysis based on data from two processes

The statistical analysis of the standard deviations σ_m of the measurement and the standard deviation σ_s of the simulation is based on the null hypothesis that the values underlying σ_m are independent and normally distributed, i.e., mitochondrial size-fluctuations are assumed to be induced by noise, only. This assumption is reasonable as the underlying numbers of σ_s are normal distributed. This statement is based on the central limit theorem (CLT, [5]) and well confirmed by our analysis (figure S1(a)). The CLT states that under certain conditions the sum of independent, identical distributed random variables approaches a normal distribution. This is an excellent approximation for a sum of 30 numbers [5]. The object size parameters d and d_y (length and width of the object, respectively) result from an averaging process over random variables and hence from a sum of random numbers: both parameters follow from the fit of the theoretical intensity distribution $I_{obj}(x, y, z = 0)$ to the measured/simulated fluorescence signal of the object. The parameters of the model object are varied until the deviation of the former from the latter is a minimum (χ^2 -minimization). This is an averaging process over the photon counting data in the images. The object intensity distribution within an image is typically distributed over more than 400 pixels. As these contain statistically independent photon counting numbers, the CLT applies.

Based on the null hypothesis, an equation for the estimation of the probability $P(\sigma_m / \sigma_s) \geq \alpha$ (see equation (1) of the main text) can be derived as follows: Let the unknown standard deviation of the normal distribution be σ and its mean zero. In a first step, we estimate the probability P as a function of a free parameter $R > 0$. Then we vary the parameter R until the estimation of P reaches an optimum.

For a given value $R > 0$ we have $\sigma_m / \sigma_s < \alpha$ if both $\sigma_m < \alpha R \sigma$ and $\sigma_s \geq R \sigma$. This yields

$$P\left(\frac{\sigma_m}{\sigma_s} \geq \alpha\right) = 1 - P\left(\frac{\sigma_m}{\sigma_s} < \alpha\right) \leq 1 - P(\sigma_m < \alpha R \sigma \wedge \sigma_s \geq R \sigma). \quad (\text{S1})$$

Taking into account the statistical independence of the measured numbers we can write

$$\begin{aligned} P\left(\frac{\sigma_m}{\sigma_s} \geq \alpha\right) &\leq 1 - P(\sigma_m < \alpha R \sigma) \cdot P(\sigma_s \geq R \sigma) \\ &= 1 - (1 - q_m) \cdot (1 - p_s) \\ &= q_m + p_s - q_m p_s \\ &< q_m + p_s, \end{aligned} \quad (\text{S2})$$

with

$$q_m = P(\sigma_m \geq \alpha R \sigma) = 1 - P(\sigma_m < \alpha R \sigma) \quad (\text{S3})$$

and

$$p_m = P(\sigma_s < R \sigma). \quad (\text{S4})$$

Hence, we have to calculate the probability $P(\sigma < k \sigma)$ for a given empirical standard deviation σ and a free parameter $k > 0$. The empirical variance σ^2 is given by

$$\sigma^2 = \frac{1}{N-1} \sum_{i=1}^N x_i^2, \quad (\text{S5})$$

with N being the number of the measured values x_i and $\langle x_i \rangle = 0$. Introducing the N -dimensional vector $\vec{x}_N = (x_1, \dots, x_N)$ yields

$$\sigma^2 = \frac{1}{N-1} \vec{x}_N^2, \quad (\text{S6})$$

with \vec{x}_N^2 being the Euclidean length. The probability $P(\sigma < k \sigma)$ is thus

$$\begin{aligned} P(\sigma < k \sigma) &= P(\sigma^2 < k^2 \sigma^2) = P(\vec{x}_N^2 < (N-1)k^2 \sigma^2) \\ &= \int_{|\vec{x}_N| < \sqrt{N-1}k\sigma} p(x_1, x_2, \dots, x_N) d\vec{x}_N \\ &= \int_{|\vec{x}_N| < \sqrt{N-1}k\sigma} p(x_1) \cdot p(x_1) \cdots p(x_N) d\vec{x}_N, \end{aligned} \quad (\text{S7})$$

where $p(x)$ is the Gaussian probability density function

$$p(x) = \frac{1}{\sigma\sqrt{2\pi}} e^{-\frac{x^2}{2\sigma^2}}. \quad (\text{S8})$$

We obtain

$$P(\sigma < k \sigma) = \frac{1}{\sqrt{2\pi\sigma^2}^N} \int_{|\vec{x}_N| < \sqrt{N-1}k\sigma} e^{-\frac{\vec{x}_N^2}{2\sigma^2}} d\vec{x}_N. \quad (\text{S9})$$

Transformation into N -dimensional polar coordinates [6] yields

$$\begin{aligned} P(\sigma < k \sigma) &= \frac{2^{1-\frac{N}{2}}}{\sigma^N \Gamma\left(\frac{N}{2}\right)} \int_0^{\sqrt{N-1}k\sigma} r^{N-1} e^{-\frac{r^2}{2\sigma^2}} dr \\ &= \frac{2^{1-\frac{N}{2}}}{\Gamma\left(\frac{N}{2}\right)} \int_0^{\sqrt{N-1}k} t^{N-1} e^{-\frac{t^2}{2}} dt, \end{aligned} \quad (\text{S10})$$

with Γ being the gamma function

$$\Gamma(x) = \int_0^\infty e^{-t} t^{x-1} dt. \quad (\text{S11})$$

The probabilities q_m and p_s thus take the form

$$q_m = 1 - \frac{2^{1-\frac{N}{2}}}{\Gamma\left(\frac{N}{2}\right)} \int_0^{\sqrt{N-1}\alpha R} t^{N-1} e^{-\frac{t^2}{2}} dt \quad (\text{S12})$$

and

$$p_s = \frac{2^{1-\frac{M}{2}}}{\Gamma\left(\frac{M}{2}\right)} \int_0^{\sqrt{M-1}R} t^{M-1} e^{-\frac{t^2}{2}} dt, \quad (\text{S13})$$

with N and M being the numbers of values obtained from experiment and simulation. Finally, the estimation of the probability $P(\sigma_m/\sigma_s \geq \alpha)$ yields (see equation (1) of the main text)

$$P\left(\frac{\sigma_m}{\sigma_s} \geq \alpha\right) < 1 - \frac{2^{1-N/2}}{\Gamma(N/2)} \int_0^{\sqrt{N-1}\alpha R} t^{N-1} e^{-t^2/2} dt + \frac{2^{1-M/2}}{\Gamma(M/2)} \int_0^{\sqrt{M-1}R} t^{M-1} e^{-t^2/2} dt. \quad (\text{S14})$$

For a given ratio $\alpha = \sigma_m/\sigma_s$ and the known numbers N and M the minimum of the right side of this equation can be calculated by varying the parameter $R > 0$ numerically, using, e.g., Mathematica (Wolfram Research, Champain, IL, USA).

Zero-crossing analysis

Zero-crossing analysis (see, e.g., [5]) was used to quantitatively analyze the persistence of observed mitochondrial size changes (see the section ‘Materials and methods’ in the main text). The noise-limited tracking precision leads to apparent mitochondrial size changes. The question to be answered here is therefore whether the observed size changes are real or brought about by the noise in the images. The measured length d_i and width d_{y_i} ($i=1\dots N$) of a mitochondrion with fixed size will be normal distributed around the mean values $\bar{d} = N^{-1} \sum_{i=1}^N d_i$ and $\bar{d}_y = N^{-1} \sum_{i=1}^N d_{y_i}$, respectively (figure S1(a) depicts an example for the normal distributed length d of a simulated mitochondrion). We can thus consider d_i and d_{y_i} ($i=1\dots N$) as a sequences of independent random variables. The probability p that noise in the images will cause an overestimated mitochondrial length $d_i > \bar{d}$ in one image and an underestimated length $d_i < \bar{d}$ in the next (or *vice versa*) is $p = 0.5$. The probability P for measuring N_0 of such size transitions (‘zero-crossings’, see figure S1(b)) in a set of N images is given by a binomial distribution

$$P(N_0, N, p) = \binom{N-1}{N_0} p^{N_0} (1-p)^{N-1-N_0}. \quad (\text{S15})$$

Figure S1(c) depicts $P(N_0)$ for $N = 100$ and $p = 0.5$. Here, the expected mean number of zero-crossings is $(N-1)p = 49.5$. Using the DeMoivre–Laplace theorem for $(N-1)p(1-p) \gg 1$ we obtain the approximation [5]

$$P(N_0, N, p) \cong \frac{1}{\sigma\sqrt{2\pi}} e^{-\frac{[N_0-(N-1)p]^2}{2\sigma^2}}, \quad (\text{S16})$$

where $\sigma = \sqrt{(N-1)p(1-p)}$. Integrating this equation with respect to N_0 from 0 to N'_0 yields the probability $P^-(N'_0)$ for measuring a zero-crossing number smaller or equal to N'_0

$$P^-(N'_0) = \frac{1}{2} \left[1 - \operatorname{erf}\left(\frac{(N-1)p - N'_0}{\sigma\sqrt{2}}\right) \right] = 1 - P^+(N'_0), \quad (\text{S17})$$

with $P^+(N'_0)$ being the probability for measuring any number of zero-crossings larger or equal N'_0 .

Supplemental information accompanying the experimental example shown in figures 2 and 3 of the main text

As the noise-limited localization precision of object borders can potentially lead to apparent mitochondrial size changes (figure 3), its effect on the FPT analysis of actively transported mitochondria has to be taken into account. This can only be achieved by computer simulations of a theoretical cargo similar to the experimental object and being transported with identical average speed whereas shape and size-parameters

are kept constant (see the above section ‘Computer simulations’). Figure S2(a) depicts the first distribution of a sequence of 100 simulated intensity distributions of a dye filled mitochondrion with identical shape and size parameters as the experimental mitochondrion shown in figure 2 of the main text. The simulated images have the same photon counting characteristics per pixel (see the inset of figure S2(a)), mean background noise I_B , standard deviation σ_{sig} of the object intensity distribution [4] and mean maximum signal above background I_0 as the experimental images (table S1).

Table S1. Representation of the image-quality determining parameters (mean \pm SD) obtained from simulation (figure S2) and underlying experiment (figure 2).

Parameter	Experiment	Simulation
SNR	4.86 \pm 0.24	4.89 \pm 0.27
I_0	5.9 \pm 0.36	6.1 \pm 0.33
σ_{sig}	1.22 \pm 0.06	1.24 \pm 0.06
I_B	0.025 \pm 0.005	0.025 \pm 0.005

The centroid of the simulated mitochondrion was displaced step by step from image to image at the same rate as given by the linearized displacement trace of the centroid of the experimental mitochondrion (figure S2(b)). Both the centroid position in the first image and the orientation of transport were the same for simulation and experiment. Figure S2(c) shows the trajectories of the characteristic object points p_0 to p_4 obtained by FPT analysis of the simulated image sequence. Analysis of the displacement traces of the centroid and the object borders with respect to the \tilde{x} - and \tilde{y} -axis of the rotated coordinate system \tilde{O} , results in the displacement traces shown in figure S2(d) (the displacement traces of the mitochondrial rear and front ends $p_1(\tilde{x})$ and $p_2(\tilde{x})$, respectively, are shown in figure 3(d) of the main text after applying a three point moving window). FPT analysis of the 100 images simulated yields the standard deviations $\sigma_d = 33.5\text{nm}$ and $\sigma_{d_y} = 30.1\text{nm}$ for the length and width of the simulated mitochondrion, respectively. Comparing these values with the standard deviations obtained from the underlying experiment, $\sigma_d = 48.6\text{nm}$ ($P < 0.009$, equation (1) with $N = M = 100$, $\alpha = 1.45$ and $R = 0.825124$) and $\sigma_{d_y} = 34.4\text{nm}$ ($P < 0.36$, equation (1) with $\alpha = 1.14$ and $R = 0.939959$), reveals significant mitochondrial length changes, whereas the standard deviations for the mitochondrial width of experiment and simulation are statistically indistinguishable.

Supplemental information accompanying the experimental examples shown in figure 4

Figures S3(a) and (b) depict the original unfiltered displacement traces of the characteristic object points $p_1(\tilde{x})$, $p_2(\tilde{x})$, $p_3(\tilde{y})$ and $p_4(\tilde{y})$ of both the apparently immobile and processively transported mitochondrion shown in figure 4 of the main text. To gain quantitative information from the noise-limited traces, we simulated image sequences of both an immobile and linear transported mitochondrion of the same shapes and sizes as the experimental mitochondria (see above section ‘Computer simulations’) (the simulated mobile mitochondrion was displaced from image to image according to the linearized movement shown in the inset of figure 4(e)). Next, we performed statistical analysis on the standard deviations of the length and width obtained from the FPT analysis of the experimental and simulated cargos. Table S2 summarizes the parameters characterizing the quality of the experimental and simulated intensity distributions.

Table S2. Representation of the image-quality determining parameters (mean \pm SD) obtained from the image sequences from the simulation (figures S3(c) and (d)) and underlying experiment (figure 4).

Parameter	Experiment (immobile mitochondrion)	Simulation (immobile mitochondrion)	Experiment (mobile mitochondrion)	Simulation (mobile mitochondrion)
SNR	9.25 \pm 0.75	10.86 \pm 0.79	7.87 \pm 0.7	8.18 \pm 0.68
I_0	33.37 \pm 1.72	33.37 \pm 0.85	20.47 \pm 1.32	20.6 \pm 0.8
σ_{sig}	3.62 \pm 0.24	3.1 \pm 0.2	2.61 \pm 0.21	2.53 \pm 0.19
I_B	0.92 \pm 0.04	0.92 \pm 0.02	0.73 \pm 0.05	0.73 \pm 0.03

Figures S3(c) and (d) show the resulting displacement traces of the object borders of the mobile and immobile mitochondrion, respectively (same color key as in figure S3(a)). FPT analysis of the simulated image sequences yields the standard deviations $\sigma_d = 24.9\text{nm}$ and $\sigma_{d_y} = 16.6\text{nm}$ for the length and width of the immobile mitochondrion and $\sigma_d = 38.4\text{nm}$ and $\sigma_{d_y} = 26.5\text{nm}$ for the length and width of the mobile mitochondrion, respectively. The comparison with the standard deviations of the length and width of the experimental immobile mitochondrion, $\sigma_d = 50\text{nm}$ ($P < 4 \times 10^{-6}$, equation (1) with $N = M = 90$, $\alpha = 2.01$ and $R = 0.682497$) and $\sigma_{d_y} = 30.1\text{nm}$ ($P < 8 \times 10^{-5}$, equation (1) with $\alpha = 1.82$ and $R = 0.724416$), and the experimental mobile mitochondrion, $\sigma_d = 66.3\text{nm}$ ($P < 3 \times 10^{-4}$, equation (1) with $\alpha = 1.73$ and $R = 0.746223$) and $\sigma_{d_y} = 53.8\text{nm}$ ($P < 3 \times 10^{-6}$, equation (1) with $\alpha = 2.03$ and $R = 0.677341$), respectively, statistically validates significant length and width changes of both mitochondria.

Further experimental examples

Forward-and-backward moving mitochondrion

Figure S4 shows an example of an oscillating, forward-and-backward moving mitochondrion. Part (a) of this figure depicts the intensity distribution together with the corresponding CLSM image of the dendritic mitochondrion. Shown is the first image of 200 sequential images. Figure S4(b) shows the result of the FPT analysis. Drawn are the displacement traces of both mitochondrial ends and the left and right mitochondrial borders (see inserted schematic for color key). The analysis reveals the sub-microscopic mitochondrion transport with frequent direction reversals. Transport is accomplished with similar mean velocities in both directions ($-0.7\mu\text{m/s} < v < 0.7\mu\text{m/s}$, figure S4(c)). Here, the noisy traces do apparently not allow to draw immediate conclusions about transport-induced mitochondrial size changes: Although the inserted smoothed trace segments in figure S4(b) might suggest non-simultaneous displacements of both cargo ends, the simulated traces clearly show similar characteristics (see inserted trace segments in figure S4(d)) (table S3 summarizes the parameters characterizing the quality of the experimental and simulated intensity distributions). Statistical analysis of the standard deviations of the mitochondrial length and width of simulation ($\sigma_d = 45.1\text{nm}$ and $\sigma_{d_y} = 44.7\text{nm}$) and experiment ($\sigma_d = 55.3\text{nm}$ and $\sigma_{d_y} = 42.8\text{nm}$) on the other hand, reveals significant mitochondrial length changes ($P < 0.0388$, equation (1) with $N = M = 200$, $\alpha = 1.23$ and $R = 0.900714$), whereas the mitochondrial width changes were statistically indistinguishable ($P < 0.667$, equation (1) with $N = M = 200$, $\alpha = 1.044$ and $R = 0.981005$). Mitochondrial size changes are thus validated exclusively along the direction of transport.

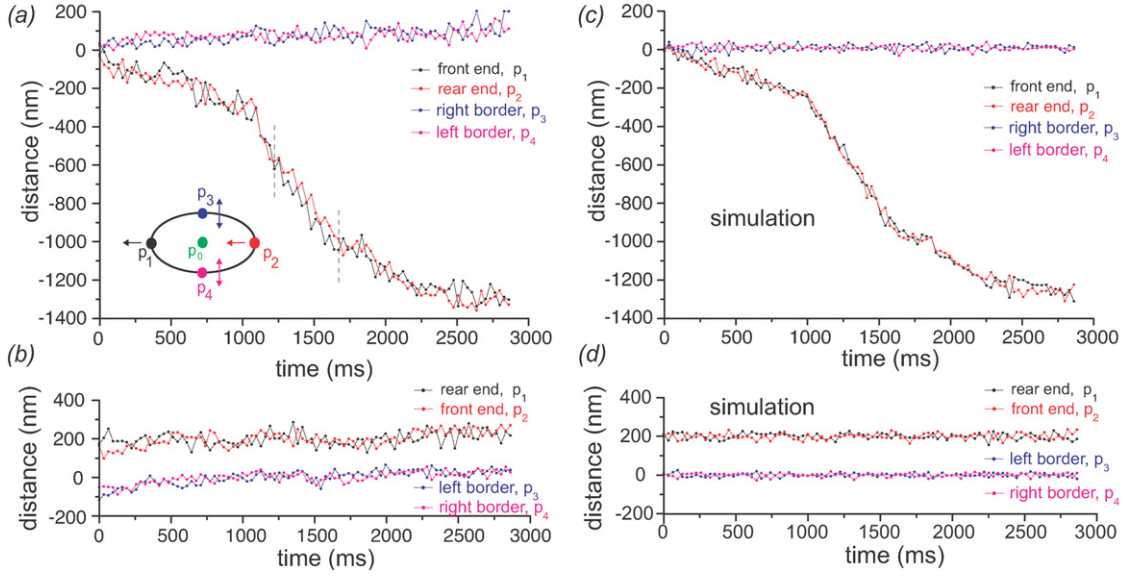


Figure S3. Measured and simulated displacement traces accompanying the experimental examples shown in figure 4 of the main text. (a) Measured displacement traces of the mobile mitochondrion. Depicted are the traces of the mitochondrial front (black trace) and rear (red trace) ends with respect to the \tilde{x} -axis of the coordinate system \tilde{O} and the left (magenta trace) and right (blue trace) mitochondrial borders with respect to the \tilde{y} -axis of \tilde{O} (see inserted schematic for color key). Prior to FPT analysis, the size of the sequential images was decreased to 88×16 pixel by removing the left part of the original images (208×16 pixel) such that the images contained only the intensity distribution of the mobile mitochondrion (see figure 4(a) of the main text). Result of the FPT analysis of the image sequence (mean \pm SD): $p = 44.35 \pm 11.02$, $d_x = 0$ (fixed), $d = d_1 + d_2 = (1577 \pm 66)\text{nm}$ ($d_1 = d_2$), $d_y = (393 \pm 54)\text{nm}$, $I_B = 0.73 \pm 0.05$, and $\varphi = -0.0398 \pm 0.0215$. (b) Displacement traces of the apparently immobile mitochondrion (for color key, see part a of this figure). Here, FPT analysis was applied to an image sequence containing only the left part (150×16 pixel) of the original images with the intensity distribution of the immobile mitochondrion. Result of the FPT analysis (mean \pm SD): $p = 36.49 \pm 3.4$, $d_x = 0$ (fixed), $d = d_1 + d_2 = (1328 \pm 50)\text{nm}$ ($d_1 = d_2$), $d_y = (631 \pm 30)\text{nm}$, $I_B = 0.92 \pm 0.04$, and $\varphi = -0.0486 \pm 0.0317$. (c) Displacement traces of the mitochondrial borders of the simulated moving mitochondrion (color key as in (a)). The underlying parameters of the simulation were the mean parameters obtained from the experiment. (d) Displacement traces of the simulated immobile mitochondrion. The parameters underlying the simulation are given above (see the caption for (b)).

Table S3. Representation of the image-quality determining parameters (mean \pm SD) obtained from simulation and underlying experiment.

Parameter	Experiment	Simulation
SNR	7.56 ± 0.69	7.7 ± 0.69
I_0	13.47 ± 1.19	14.12 ± 0.9
σ_{sig}	1.79 ± 0.23	1.8 ± 0.2
I_B	0.091 ± 0.009	0.091 ± 0.008

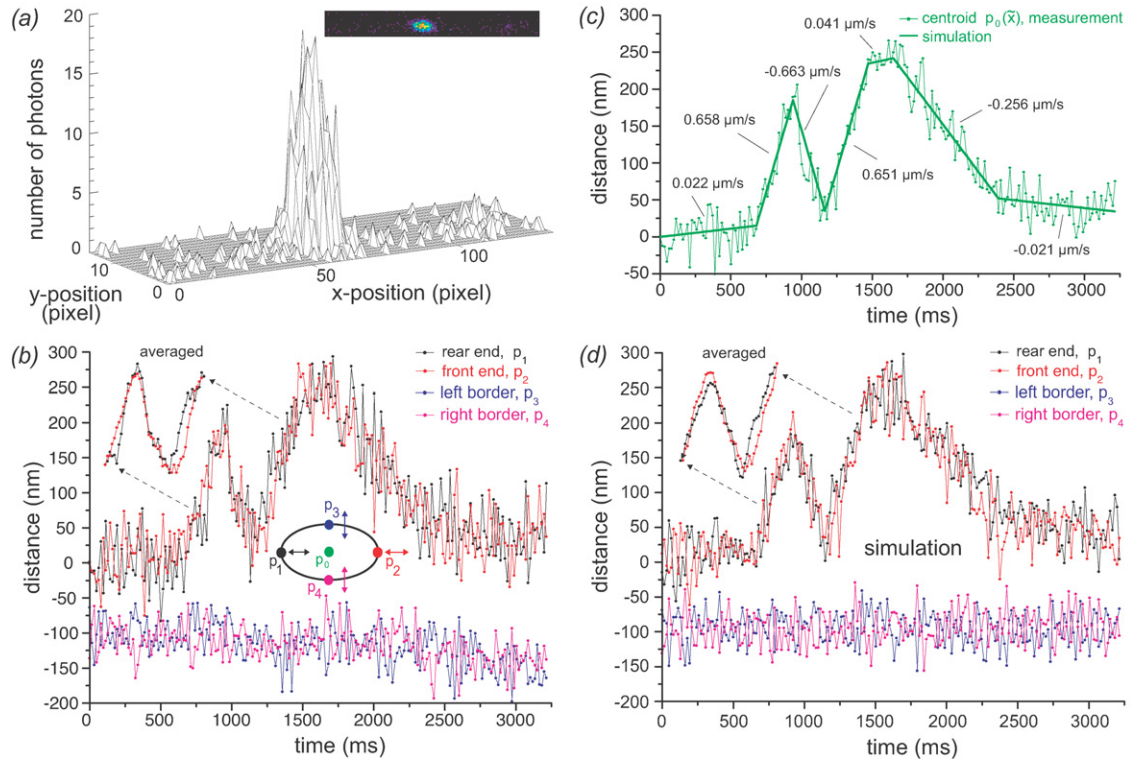


Figure S4. FPT analysis of a forward and backward moving experimental and simulated mitochondrion.

(a) Intensity distribution of the first CLSM micrograph (inset, upper right) of 100 sequential images.

Image size: 134×16 pixels. Image sampling interval: 16.16 ms. Line scanning time: 1.01 ms. Pixel dwell time: 2.55 μ s. Pixel size: 88 nm (for parameters characterizing the object intensity, see table S3).

(b) Displacement traces of the mitochondrial ends with respect to the \tilde{x} -axis of the coordinate system \tilde{O} and the left and right mitochondrial borders with respect to the \tilde{y} -axis of \tilde{O} (for clarity, both traces were shifted by 100 nm) (see inserted schematic for color key). The inserted trace segments depict a part of the original traces after applying a three point moving window. FPT analysis of the image sequence results in the following parameters (mean \pm SD): $p = 29.5 \pm 6.7$, $d_x = 0$ (fixed),

$$d = d_1 + d_2 = (1218 \pm 55) \text{ nm} \quad (d_1 = d_2), \quad d_y = (385 \pm 43) \text{ nm}, \quad I_B = 0.091 \pm 0.009, \text{ and}$$

$$\varphi = -0.08108 \pm 0.04036. \quad (c) \text{ Displacement of the centroid } (p_0) \text{ of the experimental mitochondrion}$$

along the \tilde{x} -axis of \tilde{O} . The superimposed straight lines depict the movement of the simulated

mitochondrion. The parameters underlying the simulation are given above (see the caption for (b)). (d) Displacement traces of the mitochondrial borders obtained from the FPT analysis of the simulated image sequence.

By applying the zero-crossing method, we gained further insight into the dynamics of the underlying process: The analysis revealed a significant increase in the number of zero-crossings (116, $P^+ < 0.0096$) for the mitochondrial length compared to the expected mean number of 99.5 zero-crossings, suggestive for a transport-related process (such as an ongoing tug-of-war between opposing motor molecules) that causes an increased frequency of length changes. The zero-crossing number for the mitochondrial width was found to be close to the expectation (97, $P^- < 0.36$).

Anterogradely transported mitochondrion

Figure S5 shows a further example (measurement and simulation) of a dendritic mitochondrion moving in anterograde direction. Figure S5(a) depicts the first image of 46 sequential images together with the trajectories of the four characteristic object points p_1 to p_4 (see inserted schematic in part (b)).

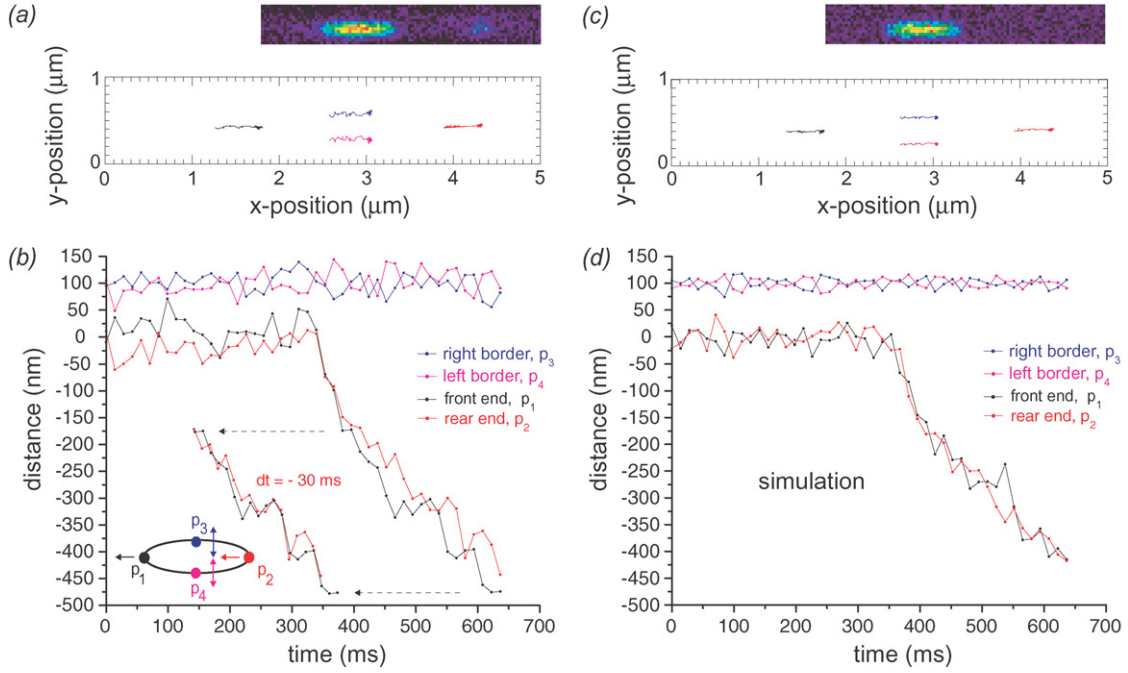


Figure S5. FPT analysis of an anterogradely transported dendritic mitochondrion. (a) First CLSM micrograph of a sequence of 46 images together with trajectories of the characteristic object points p_1 to p_4 (see inserted schematic in (b)). Image size: 99×14 pixels. Image sampling interval: 14.14 ms. Line scanning time: 1.01 ms. Pixel dwell time: $3.45 \mu\text{s}$. Pixel size: 89 nm (for parameters characterizing the object intensity, see table S4). (b) Displacement traces of the mitochondrial ends with respect to the \tilde{x} -axis of the coordinate system \tilde{O} and the left and right mitochondrial borders with respect to the \tilde{y} -axis of \tilde{O} (for clarity, both traces were shifted by 100 nm) (see inserted schematic for color key). The inserted trace segments (see dashed arrows) were superimposed by shifting the corresponding trace segment of the mitochondrial rear end along the time-axis by the indicated value. FPT analysis of the image sequence results in the following parameters (mean \pm SD): $p = 124.5 \pm 26.6$, $d_x = 0$ (fixed), $d = d_1 + d_2 = (2620 \pm 51)\text{nm}$ ($d_1 = d_2$), $d_y = (308 \pm 35)\text{nm}$, $I_B = 3.57 \pm 0.13$, and $\varphi = 0.00667 \pm 0.00571$. (c) First CLSM micrograph of the simulated sequence of 46 images together with trajectories of the characteristic object points p_1 to p_4 . The object center was displaced for each image with sub-pixel resolution along the \tilde{x} -axis of the rotated coordinate system \tilde{O} according to the mean velocities (see text) calculated from the centroid movement of the underlying experimental mitochondrion. The object position in the first image was identical to the position of the mitochondrion in the first experimental image. The parameters underlying the simulation are given above (see the caption for (b)). FPT analysis of the simulated image sequence results in the following parameters (mean \pm SD): $p = 123.4 \pm 13.6$, $d_x = 0$ (fixed), $d = d_1 + d_2 = (2619 \pm 30)\text{nm}$ ($d_1 = d_2$), $d_y = (308 \pm 18)\text{nm}$, $I_B = 3.54 \pm 0.1$, and $\varphi = 0.0072 \pm 0.0068$. (d) Displacement traces of the mitochondrial borders obtained from the FPT analysis of the simulated image sequence.

In figure S5(b) we plotted the displacement traces of the front end, the rear end, the left and the right mitochondrial borders, $p_1(\tilde{x})$, $p_2(\tilde{x})$, $p_3(\tilde{y})$ and $p_4(\tilde{y})$, respectively. The mitochondrion is immobile during the first 350 ms of data acquisition and then rapidly moves in anterograde direction with an average velocity of $3.8 \mu\text{m/s}$ and then continuous movement at $1.1 \mu\text{m/s}$. FPT analysis reveals the time-delayed displacements of both mitochondrial ends. The similarity of the movements is demonstrated by the superimposed trace segments in figure S5(b). Here, the rear end lags behind the front end with an approximate time-delay of 30 ms. Figures S5(c) and (d) depict the trajectories and displacement traces of

the characteristic object points of the corresponding simulated mitochondrion (see CLSM micrograph in figure S5(c)). Significantly, these traces do not exhibit the substantial time-delayed displacements between both mitochondrial ends that we see in the experiment (for more information underlying the simulation, see the figure caption). The persistence of the apparent length changes of the experimental mitochondrion is further statistically validated by the significantly decreased number of zero-crossings (12, $P^- < 0.001$, equation (S17)), whereas the zero-crossing number for the mitochondrial width is only slightly decreased (18, $P^- < 0.1$). Statistical analysis of the standard deviations of the mitochondrial length and width of experiment ($\sigma_d = 51.4\text{nm}$ and $\sigma_{d_y} = 35.4\text{nm}$) and simulation ($\sigma_d = 29.9\text{nm}$ and $\sigma_{d_y} = 17.8\text{nm}$) further reveals significant mitochondrial length ($P < 0.01$, equation (S14) with $N = M = 46$, $\alpha = 1.719$ and $R = 0.752688$) and width changes ($P < 0.0012$, equation (S14) with $N = M = 46$, $\alpha = 1.989$ and $R = 0.689612$). In summary, the mitochondrion exhibits significant size changes during its inchworm-like forward movement.

Table S4. Representation of the image-quality determining parameters (mean \pm SD) obtained from simulation and underlying experiment.

Parameter	Experiment	Simulation
SNR	10.87 \pm 0.56	10.75 \pm 0.55
I_0	39.71 \pm 1.79	39.49 \pm 0.78
σ_{sig}	3.66 \pm 0.26	3.68 \pm 0.2
I_B	3.57 \pm 0.13	3.54 \pm 0.1

The effect of motion blur on FPT analysis of a mobile mitochondrion

Motion blur of fluorescent mobile objects is a common problem in confocal laser-scanning microscopy. Depending on the image acquisition time and the velocity and direction of transport, shapes and sizes of mitochondria can potentially be distorted and thus complicate and bias FPT measurements [4]. Here we analyzed the effect of motion blur on the accuracy of our FPT experiments. For a given experiment we calculated, first, a sequence of noise-free CLSM images of a distorted mitochondrion being transported in the same direction and with identical mean velocities as the experimental object (assuming a line scanning time of 1 ms), and second, an image sequence of a non-distorted mitochondrion (assuming an infinitely fast image acquisition time). The fluorescence intensity of each pixel in a motion blur affected image was obtained from the intensity distribution $I_{obj}(x, y, x_0(t), y_0(t))$ of the three-dimensional model object describing the experimental mitochondrion (see the section ‘Materials and methods’ in the main text). The object center $p_0 = [x_0(t), y_0(t)]$ was displaced for each pixel with sub-pixel resolution along the \tilde{x} -axis of the rotated coordinate system \tilde{O} according to the distances calculated from the mean transport velocities and the known pixel dwell time and scanning time per line given by the underlying experiment. The object position in the first image was identical to the position of the mitochondrion in the first experimental image. A motion blur-free image was calculated based on the same intensity distribution whereas the object position was fixed for a given image and displaced between subsequent images according to the distances given by the mean transport velocities and image acquisition time of the underlying experiment. Figure S6 summarizes the results of the FPT analysis of such an image sequence for the experiment shown in figure 2 and 3 of the main text. The displacement traces of the mitochondrial front (p_2) and rear (p_1) ends of the non-distorted mitochondrion (see inserted schematic center left, dashed ellipse) are depicted by the dashed black lines. As expected, both dashed lines perfectly superimpose (only a single dashed black line is visible). Importantly, the same is true for the displacement traces of the front and rear ends of the distorted mitochondrion (solid black lines, see also inserted schematic center left, solid ellipse). Time-delayed displacements of both mitochondrial ends can not be detected on the lower nanometer scale although the displacement traces of the non-distorted and distorted mitochondrion show small deviations due to apparent length changes of the distorted mitochondrion (solid green line). To visualize the effect of motion blur directly, we inserted intensity distributions of the distorted mitochondrion calculated for three different velocities (see lower corner right). For the parameters of the underlying experiment, the difference between the distributions of an immobile and at $2\mu\text{m/s}$ transported mitochondrion can hardly be seen by eye. The length deviations from the exact mitochondrial length (green dashed line) strongly depend on both the

speed and direction of transport. The maximum error is less than 3 nm at the maximum speed of $-2\mu\text{m/s}$ and is thus neglectable for our purposes (the error corresponds to less than 0.3% of the total length of the mitochondrion of 1178 nm). The maximum error decreases below 0.4 nm when the mitochondrion is transported parallel to the x -axis of the coordinate system O ($\alpha = 0^\circ$, red solid line). Based on the above analysis, artifacts due to motion blur can be excluded. As exemplified for the measurement in figure 2 of the main text, the same conclusion followed from all experiments discussed herein.

Reinterpretation of recent single-particle tracking (SPT) data on bidirectional peroxisome transport

In a recent study [7], Kural *et al* report that both conventional kinesin and cytoplasmic dynein take ~ 8 nm steps along microtubules when carrying a peroxisome in processes of cultured S2 cells. Based on their observation that step sizes were never smaller than this they argue against a tug-of-war scenario. The authors' arguments are based on the putative compliant motor–peroxisome linkage, which they suggest would cause a degradation of step sizes if motor proteins with opposite directionality work simultaneously.

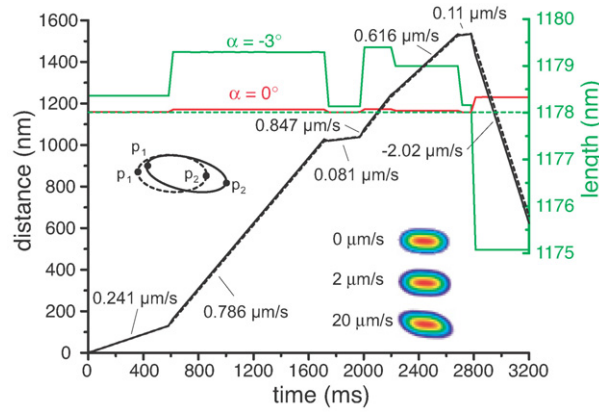


Figure S6. Effect of motion blur on FPT analysis of a linear transported mitochondrion (the corresponding experiment is shown in figure 2 of the main text). The dashed black lines show the displacement traces of the front and rear ends of the non-distorted mitochondrion (only a single dashed black line is visible), whereas the displacement traces of the front and rear ends of the distorted mitochondrion are given by the solid black lines (for information regarding the calculation of both image sequences, see text). The object parameters underlying the calculation are the mean parameters obtained from the experiment shown in figure 2 of the main text (see the caption for figure S2(b)). FPT analysis of the image sequence of the non-distorted object results in a constant object length (dashed green line), whereas the measured length of the distorted mitochondrion changes with the speed of transport (solid green line). The solid red line depicts the length changes for the same mitochondrion moving along the x -axis of the coordinate system O ($\alpha = 0^\circ$).

Here we demonstrate that the same data can also be interpreted in favor of a model partially based on a tug-of-war between motor proteins, an interpretation in agreement with the observations reported in our study. We consider two alternative scenarios, one in which the motor–peroxisome linkage relaxes between motor steps (scenario 1) (applies to the author's interpretation of the data) and another in which the motor–peroxisome linkages are continuously stretched taut during processive unidirectional movement and direction reversals (scenario 2). Based on a few calculations, we will demonstrate that the second scenario is more likely to account for the reported observations, which finally leads us to a tug-of-war interpretation (for the sake of simplicity we assume here, as suggested by Kural *et al* [7], that one kinesin and one dynein molecule, respectively, was responsible for the microtubule plus- and minus-end directed peroxisome transport shown in figure 2 of their publication).

Scenario 1. The motor–peroxisome linkage relaxes between steps

This scenario requires that the force on the motor–peroxisome linkage becomes negligible between consecutive motor steps. Let us begin our discussion with an unstretched kinesin-1 molecule positioned in front of the peroxisome, ready to pull it forward, as in the case of a motor step in a row of consecutive

unidirectional 8 nm steps (the first motor step(s) after a direction reversal with an arbitrarily positioned motor molecule will be discussed next). We first demonstrate that the motor–peroxisome linkage becomes potentially significantly stretched at the beginning of a step. Then, we calculate the time needed to release the elastic energy stored in the elongated motor–peroxisome linkage and compare the results with the observations reported by Kural *et al* [7].

When the motor takes a step, its linkage to the peroxisome becomes stretched due to the opposing drag force on the peroxisome. The degree of the elongation of the kinesin–peroxisome linkage depends on the maximum force developed during the step. As the rising ‘edge’ of steps could not be detected in the authors’ SPT experiments despite the increased time resolution of 1.1 ms [7], it is reasonable to assume that motor steps occurred with a time constant potentially as fast as in buffer ($t < 50 \mu\text{s}$ in case of kinesin-1; see, [8, 9]) (a significantly larger time constant such as $500 \mu\text{s}$ would allow the detection system to sample a point of the rising edge of every step that occurs, in particular, the first detected displacement after the beginning of a step should always be smaller than $[1 - \exp(-1.1/0.5)] \times 8\text{nm} = 7.1\text{nm}$). The required maximum force to move a 200 nm vesicle in a viscous cytoplasm within $\sim 50 \mu\text{s}$ 8 nm forward is 16 pN [10]. A force of 16 pN seems to be at odds with kinesins stall force of 5-7 pN [11]. However, note that the stall force is measured in an optical trapping assay where the motor feels a continuous load in contrast to the maximum force during a step that is needed only for a small fraction (1%) of the enzymatic cycle [10]. Considering both the proposed maximum force of 16 pN and the reported maximum stiffness of a kinesin–bead linkage of 0.3-0.6 pN/nm [9, 12, 13], an elongation of the kinesin–peroxisome linkage is not an unlikely scenario (the same idea applies to the dynein–peroxisome linkage, see below). Importantly, a force close to kinesins stall force will be sufficient to stretch a kinesin–bead linkage taut [9, 12, 14]. However, the exact elongation of the kinesin–peroxisome linkage is hard to predict, first, due to the nonlinear nature of kinesins’ compliance [8, 9, 12, 14, 15], second, due to the unknown series compliance of the peroxisome membrane, and third, as the required maximum force strongly depends on the unknown *in vivo* time constant of the steps. Also, the compliance of the motor–peroxisome linkage might be decreased *in vivo* (compared to the motor–bead linkage in optical trapping experiments) when motors become attached to the peroxisome *via* motor-binding proteins [16].

In case of dynein, we can further substantiate the assumption of a stretched motor–peroxisome linkage based on experimental data. The authors report that the dimeric cytoplasmic dynein takes 8 nm steps when it transports a peroxisome towards the minus-end of a microtubule, consistent with movement under load close to dyneins stall force of 1.1 pN [17]. Considering the reported stiffness of monomeric dynein of 0.1-0.3 pN/nm [18, 19], a produced maximum force close to 1.1 pN will easily cause a stretching of the dynein–peroxisome linkage. In conclusion, the first scenario predicts that the motor–peroxisome linkage becomes significantly stretched when it moves a peroxisome 8 nm forward.

The elastic energy stored in the elongated motor molecule will then be released during the following dwell time. As neither the rising edge of steps has been detected nor any significant peroxisome movement has been observed between consecutive motor steps (see figure 2(a) in [7]), the peroxisome must follow the motor molecule to its new position in significantly less than 1.1 ms after the initial motor step (see above). If we represent the motor–peroxisome linkage by an elastic linear spring with spring constant k , the time τ that the peroxisome needs to relax to its new equilibrium position is given by $k_B T / Dk$, with $D = k_B T / 6\pi\eta r$ being the diffusion constant of the peroxisome, k_B the Boltzmann’s constant and T the temperature (see, e.g., [20]). A peroxisome with a radius r between 100 to 200 nm [21] has a diffusion constant in the range of $9.4 \cdot 10^{-12}$ to $18.9 \cdot 10^{-12} \text{cm}^2/\text{s}$ in a cytoplasm with viscosity $\eta = 1.1 \text{Pa} \cdot \text{s}$ [22, 23] and a temperature of 10 °C (283.15K). Assuming a stiffness of 0.3–0.6 pN/nm for the kinesin–peroxisome linkage and 0.1–0.3 pN/nm for the dynein–peroxisome linkage, we obtain a range for the relaxation time of 4 to 14 ms and 7 to 42 ms for a peroxisome transported by a single kinesin and dynein, respectively. These ranges presumably reflect the lower limits of relaxation times as a potential size and shape change of the peroxisome (caused by the pulling of the motor) will contribute a series compliance, as the stiffness of the motor–peroxisome linkage will decrease with relaxation (shown for the kinesin–bead linkage, [13]), and as the chosen cytoplasmic viscosity has been measured at 37 °C [22] and will be increased at 10°C [23]. It seems thus to be unlikely that a peroxisome can follow a motor molecule to its new position within significantly less than 1.1 ms.

Before we continue with the discussion of the second scenario of a continuously stretched taut motor–peroxisome linkage, we consider the first motor step(s) in row of unidirectional steps, e.g., the first step(s)

of cytoplasmic dynein after a direction reversal. In this case, the motor molecule is arbitrarily positioned with respect to the cargo. Due to the random attachment position of the dynein cargo binding domain somewhere on the peroxisome surface and the binding of dynein's stalk head to a microtubule binding site not necessarily located in front of the peroxisome, the first step(s) or displacement(s) of the peroxisome should be distinct from the observed 8 nm displacements: The average distance d that a dynein molecule of length l has to move before a force is imposed on the peroxisome with radius r is equal to $d = (r + l)\cos\alpha$, with $\alpha = \arcsin[r/(r + l)]$. With a dynein length of ~ 35 nm [24] and a peroxisome radius of 100 nm, we obtain an average distance of 91 nm. Assuming 8 nm motor steps [7], dynein would have to take on average 11 steps before it reaches an optimal position in front of the peroxisome. Thus, the initial motor steps should cause some kind of peroxisome movement that is distinct from the observed 8 nm steps. As no significant peroxisome movement between direction reversals has been reported (see figure 2(c) in [7]), it is reasonable to assume that the peroxisome movement is severely restricted by the surrounding cytoskeletal filaments or/and attached motor molecules (see below). This in turn is consistent with the proposed high forces that are needed to move a peroxisome forward. However, our kinetic considerations (see above), which are based on high initial forces, make it unlikely that scenario 1 accounts for the reported observations. We thus consider the second scenario of a continuously stretched taut motor–peroxisome linkage.

Scenario 2. Continuously stretched taut motor–peroxisome linkage

A continuously stretched taut motor–peroxisome linkage during unidirectional movement can potentially be achieved in three different ways. First, the peroxisome could feel a constant drag force of $F = 6\pi\eta r v$ [22], where v is the peroxisome velocity. For a peroxisome with a radius between 100 to 200 nm and a viscosity of 1.1 Pa·s, the required motor force for transporting a peroxisome at $2.4\mu\text{m/s}$ (see upper trace of figure 2(a) in [7]) is in the range of 5 to 10 pN. A load close to 5 pN will be sufficient to elongate a motor molecule [9, 14]. However, a constant drag force seems to be at odds with the observation that the peroxisome velocity becomes negligible between consecutive steps (figure 2 in [7]). A second explanation could be the intracellular network of cross-linked microtubules that might prevent the peroxisome from following the motor closely and hence creates an elongated motor–peroxisome linkage. This idea would be consistent with a strongly viscoelastic and heterogeneous cytoplasm (a bimodal distribution of loads has recently been suggested [25]). When the motor takes a step, it increases the imposed force on the peroxisome and eventually pulls the peroxisome forward by braking bonds between microtubules such as the interconnections *via* tau until the cargo encounters the next obstacles. However, both the viscous cytoplasm and the network of cross-linked microtubules will not be capable of maintaining a stretched taut motor–peroxisome linkage during direction reversals, the first step of the opposite polarity motor will still begin with an unstretched motor–peroxisome linkage. We thus consider the third explanation, which is based on the activity of opposing motors:

The requirement of a stretched taut motor–peroxisome linkage leads to arguments against a mechanism of motor coordination in which kinesin is deactivated first and dynein becomes activated in a succeeding step. In contrast, either a motor coordination model in which, e.g., dynein is activated before kinesin becomes inactive (to ensure a stress on the dynein–peroxisome linkage), followed by the inactivation of kinesin (a model partially based on tug-of-war) or a mechanism solely based on tug-of-war between dynein and kinesin (less likely, [26]) could explain the reported observations. If a peroxisome-attached dynein would begin to step in minus-end direction while kinesin still tries to walk in plus-end direction under stretched taut condition, the dynein–peroxisome linkage would become elongated under increasing load without any detectable degradation of the plus-end directed 8 nm steps (kinesins steps are not significantly degraded under stretched taut conditions, see [9, 14]). Kinesin could become inactivated (e.g., by a motor cofactor protein that senses strain in the cargo membrane) or stall (if the number of pulling dyneins is high enough) or even be forced to move processively backwards under a load well above its stall force [9]. Obviously, these processes have to occur sufficiently fast to be consistent with the reported observations.

In summary, with a few assumptions based on published data, it is possible to reinterpret the single-particle tracking data presented by Kural and co-workers in favor of a model partially based on tug-of-war between opposing motors and thus highlights the need for direct evidence for the mechanism underlying bidirectional organelle transport.

References

- [1] Bischofberger J and Schild D 1995 Different spatial patterns of $[\text{Ca}^{2+}]$ increase caused by N- and L-type

- Ca²⁺ channel activation in frog olfactory bulb neurons *J. Physiol.* **487** 305–17
- [2] Nieuwkoop P D and Faber J 1956 *Normal Table of Xenopus laevis (Daudin)* (Amsterdam: North Holland)
- [3] Ligon L A and Steward O 2000 Movement of mitochondria in the axons and dendrites of cultured hippocampal neurons *J. Comp. Neurol.* **427** 340–50
- [4] Gennerich A and Schild D 2005 Sizing-up finite fluorescent particles with nanometer-scale precision by convolution and correlation image analysis *Eur. Biophys. J.* **34** 181–99
- [5] Papoulis A and Pillai S U 2002 *Probability, Random Variables, and Stochastic Processes* 4th edn (New York: McGraw-Hill)
- [6] Fichtenholz J 1964 *Differential- und Integralrechnung III* (Berlin: VEB Deutscher Verlag der Wissenschaften)
- [7] Kural C, Kim H, Syed S, Goshima G, Gelfand V I and Selvin P R 2005 Kinesin and dynein move a peroxisome *in vivo*: a tug-of-war or coordinated movement? *Science* **308** 1469–72
- [8] Nishiyama M, Higuchi H and Yanagida T 2002 Chemomechanical coupling of the forward and backward steps of single kinesin molecules *Nat. Cell Biol.* **4** 790–7
- [9] Carter N J and Cross R A 2005 Mechanics of the kinesin step *Nature* **435** 308–12
- [10] Holzwarth G, Bonin K and Hill D B 2002 Forces required of kinesin during processive transport through cytoplasm *Biophys. J.* **82** 1784–90
- [11] Visscher K, Schnitzer M J and Block S M 1999 Single kinesin molecules studied with a molecular force clamp *Nature* **400** 184–9
- [12] Kojima H, Muto E, Higuchi H and Yanagida T 1997 Mechanics of single kinesin molecules measured by optical trapping nanometry *Biophys. J.* **73** 2012–22
- [13] Kawaguchi K, Uemura S and Ishiwata S 2003 Equilibrium and transition between single- and double-headed binding of kinesin as revealed by single-molecule mechanics *Biophys. J.* **84** 1103–13
- [14] Svoboda K, Schmidt C F, Schnapp B J and Block S M 1993 Direct observation of kinesin stepping by optical trapping interferometry *Nature* **365** 721–7
- [15] Svoboda K and Block S M 1994 Force and velocity measured for single kinesin molecules *Cell* **77** 773–84
- [16] Kamal A and Goldstein L S 2002 Principles of cargo attachment to cytoplasmic motor proteins *Curr. Opin. Cell Biol.* **14** 63–8
- [17] Mallik R, Carter B C, Lex S A, King S J and Gross S P 2004 Cytoplasmic dynein functions as a gear in response to load *Nature* **427** 649–52
- [18] Sakakibara H, Kojima H, Sakai Y, Katayama E and Oiwa K 1999 Inner-arm dynein c of *Chlamydomonas* flagella is a single-headed processive motor *Nature* **400** 586–90
- [19] Lindemann C B and Hunt A J 2003 Does axonemal dynein push, pull, or oscillate? *Cell Motil. Cytoskeleton* **56** 237–44
- [20] Chen Y, Yan B and Rubin R J 2002 Fluctuations and randomness of movement of the bead powered by a single kinesin molecule in a force-clamped motility assay: Monte Carlo simulations *Biophys. J.* **83** 2360–9

- [21] Alberts B, Johnson A, Lewis J, Raff M, Roberts K and Walter P 2002 *Molecular Biology of the Cell*. Fourth Edition (New York: Garland)
- [22] Hill D B, Plaza M J, Bonin K and Holzwarth G 2004 Fast vesicle transport in PC12 neurites: velocities and forces *Eur. Biophys. J.* **33** 623–32
- [23] Howard J 2001 *Mechanics of Motor Proteins and the Cytoskeleton* (Sunderland, MA: Sinauer Associates Inc.)
- [24] Samso M, Radermacher M, Frank J and Koonce M P 1998 Structural characterization of a dynein motor domain *J. Mol. Biol.* **276** 927–37
- [25] Schnitzer M J, Visscher K and Block S M 2000 Force production by single kinesin motors *Nat. Cell Biol.* **2** 718–23
- [26] Gross S P 2004 Hither and yon: a review of bi-directional microtubule-based transport *Phys. Biol.* **1** R1–11